

The Influence of Coupled Sea Surface Temperatures on the Madden–Julian Oscillation: A Model Perturbation Experiment

DUANE E. WALISER

Institute for Terrestrial and Planetary Atmospheres, State University of New York at Stony Brook, Stony Brook, New York

K. M. LAU

Climate and Radiation Branch, Goddard Space Flight Center, National Aeronautics and Space Administration, Greenbelt, Maryland

JAE-HOON KIM

Space Applications Corporation, Vienna, Virginia

(Manuscript received 28 May 1997, in final form 12 March 1998)

ABSTRACT

In this study, the authors compare the Madden–Julian oscillation (MJO) variability in the Goddard Laboratory for Atmospheres atmospheric general circulation model for two different sea surface temperature (SST) boundary conditions. In the “control” simulation, the model employs specified annual cycle SSTs. In the “coupled” simulation, the model employs the same annual cycle SSTs but in addition is coupled to a slab ocean mixed layer that provides prognostic SST anomalies equatorward of 24° . The results show that the simplified interactive SST facilitates a better simulation with respect to a number of general model shortcomings associated with the MJO that were recently documented by Slingo et al. in an Atmospheric Model Intercomparison Project study. These improvements include 1) increased variability associated with the MJO, 2) a tendency for the timescales of the modeled intraseasonal variability to more closely match and consolidate around the timescales found in the observations, 3) a reduced eastward phase speed in the Eastern Hemisphere, and 4) an increased seasonal signature in the MJO with relatively more events occurring in the December–May period.

The above changes are associated with a systematic change in SST, with warming of about 0.10° – 0.15°C before the passage of the MJO convection center and cooling of the same magnitude after its passage, both of which appear to be roughly consistent with observations. These changes in SST are primarily due to decreased latent heat flux ($\sim 25 \text{ W m}^{-2}$) and slightly enhanced surface shortwave flux ($\sim 10 \text{ W m}^{-2}$) to the east of the convection, enhanced latent heat flux and diminished shortwave flux ($\sim 25 \text{ W m}^{-2}$) coincident with the convection, and enhanced latent heat flux ($\sim 25 \text{ W m}^{-2}$) just west of the convection. The results indicate that the enhanced SST to the east of the convection reinforces the meridional convergence associated with the frictional wave–CISK (conditional instability of the second kind) mechanism that appears to be at work within the model. This enhanced meridional convergence transports more low-level moisture into the region lying just east of convection. The resulting increase in moist static energy helps destabilize the disturbance and/or maintain it against dissipation more effectively relative to the case without SST coupling. The above results are discussed in terms of their relation to current MJO theory, as well as to their implications for medium- to extended-range weather forecasting.

1. Introduction

The Madden–Julian oscillation (MJO; Madden and Julian 1971) represents the most significant form of atmospheric variability in the Tropics on intraseasonal timescales. Since its discovery in the early 1970s, a wealth of studies have been undertaken to characterize its space–time structure, theorize its origin, and simu-

late/forecast its behavior in numerical models. The observational studies of the MJO have recently been reviewed by Madden and Julian (1994).¹ Briefly, these studies have resulted in the following description. The MJO is generally manifested as an eastward propagat-

Corresponding author address: Dr. Duane E. Waliser, Inst. for Terrestrial and Planetary Atmospheres, State University of New York, Stony Brook, NY 11794-5000.
E-mail: waliser@terra.msrb.sunysb.edu

¹ These studies include but are not limited to Madden and Julian (1971, 1972), Murakami (1976), Yasunari (1979, 1980), Lau and Chan (1983, 1985, 1986), Weickmann (1983), Nakazawa (1986), Knutson and Weickmann (1987), Chen and Murakami (1988), Chen et al. (1988), Gray (1988), Hendon and Liebmann (1990a, b), Wang and Rui (1990a), Lau et al. (1991), Hendon and Salby (1994), and Salby and Hendon (1994).

ing, equatorially trapped, wavenumber-one, baroclinic oscillation in the tropical wind field. The propagation speed is on the order of 6 m s^{-1} in the Eastern Hemisphere where it strongly interacts/modulates deep convective activity, and about 12 m s^{-1} or greater in the Western Hemisphere where it continues to propagate without much influence on the cloud field. Interactions between MJO-related anomalies in convection and the large-scale circulation are strongest in the Eastern Hemisphere, over the Indian and western Pacific Oceans, where the oscillation exhibits its greatest variability and typically reaches its maximum amplitude. Such interactions strongly influence the onset and activity of the Asian–Australian monsoon system (e.g., Yasunari 1979, 1980; Hendon and Liebmann 1990a, 1990b) and have also been shown to influence extratropical regions as well (e.g., Weickmann 1983; Liebmann and Hartman 1984; Weickmann et al. 1985; Lau and Philips 1986; Ferranti et al. 1990). Furthermore, coupling with the tropical ocean via westerly wind bursts associated with the passage of an MJO convection event can significantly modify the structure of the thermocline in the equatorial Pacific Ocean (e.g., McPhaden and Taft 1988; Kessler et al. 1996). This latter interaction has even been suggested to play an important role in triggering El Niño–Southern Oscillation (ENSO) events (e.g., Lau and Chan 1988; Weickmann 1991; Kessler et al. 1996).

While the observational description of the MJO has progressed steadily in the last two decades, theoretical understanding of the MJO has faced some difficulties. Most difficult has been explaining the slow eastward propagation in conjunction with the low (zonal) wavenumber structure (e.g., Hayashi and Golder 1993). Variations of wave–CISK (conditional instability of the second kind) have been the basis for one line of theory. Wave–CISK theory proposes that low-level moisture convergence induces deep cumulus convection, and the latent heat release due to condensation forces unstable eastward propagating modes (e.g., Chang 1977; Lau and Peng 1987; Chang and Lim 1988; Hendon 1988). These modes induce further low-level convergence, and thus latent heating, to the east of the original region of latent heat release, and so forth. Despite the initial success of wave–CISK in simulating the eastward propagation, the phase speeds of the unstable modes were typically higher than observed. In addition, wave–CISK models often exhibited scale selection problems in which the shortest waves are the most unstable in the linear case, while in the nonlinear case, the convection region tends to favor the smallest (i.e., grid) scales (e.g., Crum and Dunkerton 1994; Chao 1995). However, these unfavorable features tend to be remedied when the wave–CISK model allows for coupling to a frictional boundary layer (Wang 1988a; Salby et al. 1994) and coupling between moist Kelvin and Rossby modes (Wang and Rui 1990a). Hendon and Salby (1994, 1996) have shown strong evidence that each of these types of coupling tend to occur in the

observed features of the MJO in the Eastern Hemisphere as it propagates east.

In contrast to the (frictional) wave–CISK mechanism, the evaporation–wind feedback theory for the MJO (Emanuel 1987; Neelin et al. 1987) claims that diabatic heating due to cumulus convection is nearly compensated by adiabatic cooling. Further, a region of anomalous convection forces low-level easterly winds to the east and low-level westerly winds to the west of the convective region. If the convection is present in a region of mean easterly winds, the strength of the wind speed anomalies (and likely the evaporation anomalies) is increased to the east and decreased to the west of the convective region. The positive anomalies of surface latent heat flux to the east of the convection increase the low-level moist static energy, which leads the wave vertical velocity and induces unstable eastward propagating modes. The evaporation–wind feedback theory has been criticized based on the fact that over a large portion of the Eastern Hemisphere where the MJO is most prevalent, the climatological winds are extremely weak or even westerly (Wang 1988b). Neelin (1988) and Emanuel (1988) have argued that given the large zonal scale of the MJO convective feature, the requirement for (stronger) mean easterlies to the east of the convection (compared to the weak/westerly winds to the west) typically holds in most cases of convection occurring in the eastern Indian Ocean and western Pacific.

An even more imposing difficulty facing the evaporation–wind feedback theory comes from recent studies that document the observed relation between deep convection and evaporation associated with the MJO. A number of recent studies have shown that evaporation anomalies are typically higher to the west, rather than to the east, of the convection anomaly (e.g., Jones and Weare 1996; Lin and Johnson 1996; Lau and Sui 1997; Jones et al. 1998), which is at odds with one of the central premises of the evaporation–wind feedback theory. Additional theoretical attempts include those by Kirtman and Vernekar (1993), who examined a simplified model that contains both the wave–CISK and evaporation–wind feedback mechanisms with the result that model wave speeds were found to match the observed speeds over a wider range of parameter values for the combined mechanism than for evaporation–wind feedback acting alone. In addition, Hu and Randall (1994, 1995) have examined the possibility that the intraseasonal oscillations may partly stem from local radiative–convective oscillations, leading to a standing oscillation. However, Zhang and Hendon (1997) have demonstrated that no dominant standing component is evident in the observations and that tropical intraseasonal variability is dominated by eastward traveling components.

One aspect that has received little theoretical attention concerns the role an interactive sea surface temperature (SST) has on the character and maintenance of the MJO. All variations of the theories discussed above assume

that SST remains fixed, and thus coupled processes between MJO-modulated surface heat fluxes and the SST are not accounted for. However, there has been increasing observational evidence that significant variability in surface heat fluxes and SST do exist at intraseasonal timescales (e.g., Krishnamurti et al. 1988; Kawamura 1988; Zhang 1996; Lau and Sui 1997; Jones et al. 1998; Sperber et al. 1997). In some of the more recent studies, composite surface conditions associated with the MJO, including flux components, are produced and analyzed. For example, Zhang (1996) used Tropical Ocean Global Atmosphere (TOGA) Tropical Atmosphere–Ocean array data, Lau et al. (1996) used TOGA Coupled Ocean–Atmosphere Response Experiment (COARE) events and observations, while Jones et al. (1998) used fluxes derived from about 10 years of satellite data and European Centre for Medium-Range Weather Forecasts (ECMWF) surface analyses. The relationships between SST and convective activity documented in these studies suggest the possibility of a positive feedback in which SST variations may strengthen the power of the oscillation and influence its eastward propagation, an idea that was noted several years ago in an observational study of outgoing longwave radiation (OLR) and SST by Kawamura (1991; cf. Li and Wang 1994; Waliser 1996; Jones and Weare 1996; Flatau et al. 1997; Lau and Sui 1997; Sperber et al. 1997).

In a related context, Lau and Shen (1988), and Hirst and Lau (1991) developed a coupled ocean–atmosphere dynamical framework that included an SST-coupled tropical intraseasonal oscillation as a possible mechanism for interacting with ENSO. Particularly relevant to the discussion here is their finding that for SST exceeding 28°C, there is a large increase in coupled SST–intraseasonal oscillation instability (cf. Wang and Rui 1990b; Li and Wang 1994). They suggested that this enhanced instability could lead to more frequent/intense intraseasonal oscillations (and westerly wind bursts), which in turn could help trigger El Niño events. More recently, Wang and Xie (1998) have developed a theoretical framework similar to that in Lau and Shen (1988) and Hirst and Lau (1991), except that it explicitly includes mixed layer processes in addition to the ocean dynamical processes. The results of that study show that the mixed layer processes tend to destabilize high-frequency phenomena (e.g., MJO) and that ocean dynamics destabilize the low-frequency phenomena (i.e., ENSO). In view of the above theoretical results, along with the recent observations regarding the relationships between the MJO and SST discussed above, the physical basis for the interaction between SST and the intraseasonal oscillation needs further examination. Moreover, given the uncertainties and shortcomings in the theoretical treatment of the MJO, it is not surprising that numerical simulations of the MJO are still inadequate. As part of the Atmospheric Model Intercomparison Project (AMIP; Gates 1992), Slingo et al. (1996) have recently compared the MJO variability in 15 general circulation

models (GCMs) to the observed variability as represented by the ECMWF analyses. Their analysis showed that the most consistent shortcoming among the models is the weak representation of the strength of the intraseasonal variability. Secondary to this feature, the models generally had difficulty representing

- the slower phase speed in the Eastern Hemisphere versus the Western Hemisphere;
- the prominence of a spectral peak in 200-mb velocity potential and zonal wind at 50–60 days with a secondary peak at 25–30 days;
- the observed coherent structure of the propagating zonal wind anomalies along the equator;
- the strong tendency for most equatorially propagating disturbances to occur in the December–May period;
- the relative weakness of the high-frequency, low-wavenumber variability relative to the low-frequency, low-wavenumber variability;
- the observed ratio between seasonal to intraseasonal variance in the upper-level zonal wind field; and
- the observed influence of interannual variability on the frequency and intensity of the MJO.

Given that the MJO in the observations (i.e., analyses) manifests itself within the coupled ocean–atmosphere system yet those in the model simulations manifest themselves in an environment with a fixed SST, some of the inadequacies of the model simulations may result from the lack of interaction with a coupled/variable SST. In this article, we present results that suggest that this may indeed be the case. In fact, the results show that an interactive SST may facilitate a better model simulation of the MJO with respect to the first five of the above listed items.

We would like to stress that the numerical side of this issue has been investigated very little. The only other study has been by Flatau et al. (1997), which employed a five-layer, idealized, R15 atmospheric model over an “aquaplanet” with a simplified surface energy budget and ocean mixed layer feedback. The results in that study led Flatau et al. to conclude that the MJO was more accurately depicted as a coupled phenomena, an assessment echoed in the fixed-SST modeling and observational study by Sperber et al. (1997). Such conclusions, along with the overwhelming amount of observational evidence now available indicating fairly strong interactions in the warm pool regions between the atmosphere and SST at MJO timescales, suggest that the problem should be examined in the context of a more sophisticated atmospheric model. Furthermore, we would like to emphasize that even with the advent of several fully coupled ocean–atmosphere models, the authors are not aware of any published MJO-related studies undertaken with such models. In any case, there are good reasons why such studies would have to be approached with extreme care in order to distill the effects of an interactive SST alone on the MJO. These reasons, along with the atmospheric model and experimental set-

up, are discussed in the next section. In section 3, we present the results of the experiments. In section 4, we discuss the results, the primary physics that appear to underlie the change in the MJO, and connections to related studies. In section 5, we conclude with a summary, discuss some practical matters with regards to undertaking this and future such modeling studies, and discuss the impact the results may have on medium- to extended-range weather forecasting.

2. Model and experiments

The model used in these experiments is the Goddard Laboratory for the Atmospheres (GLA) GCM. This model was derived from an earlier version described by Kalnay et al. (1983). Modifications have included increased vertical resolution and several changes in the parameterizations of radiation, convection, cloud formation, precipitation, vertical diffusion, and surface processes (cf. Sud and Walker 1992; Phillips 1996). The horizontal representation uses finite differences on a 4° lat \times 5° long energy- and momentum-conserving A grid (Arakawa and Lamb 1977). The horizontal advection of atmospheric variables is accurate to fourth order (Kalnay et al. 1983). The vertical domain has 17 unequally spaced sigma levels extending from the surface to about 12 hPa. At every dynamical time step, a 16th-order Shapiro (1970) filter (with timescale 90 min) is applied to the prognostic fields; a Fourier filter is also applied in polar latitudes. Negative moisture values are filled by “borrowing” moisture from the level below, and from neighboring horizontal grid boxes at the lowest vertical level. Horizontal diffusion is not included and the effects of vertical diffusion are treated by the level-2.5 second-order turbulence closure model of Helfand and Labraga (1988). The planetary boundary layer (PBL) is defined by the first three levels above the surface (at $\sigma = 0.994, 0.971$, and 0.930). Near the surface, the PBL is treated as an extended surface layer and a viscous sublayer in the space between the surface and the tops of the surface roughness elements. Appropriate parameterizations are utilized to determine turbulent fluxes in the different PBL subregions. Both seasonal and diurnal cycles in solar forcing are simulated with atmospheric radiation treated as in Harshvardhan et al. (1987). The formulation of convection follows the scheme of Arakawa and Schubert (1974), as implemented in discrete form by Lord and Arakawa (1980). The model orography is based on the $1^\circ \times 1^\circ$ topographic height data of Gates and Nelson (1975) that have been area averaged over the $4^\circ \times 5^\circ$ grid boxes. The resulting orography is smoothed using a 16th-order Shapiro (1970) filter, and a Fourier filter poleward of 60° latitude. Negative terrain heights resulting from the smoothing process are set to zero. Land surface processes are simulated as in the Xue et al. (1991) modification of the model of Sellers et al. (1986).

In general, the GLA model fared quite well with

respect to its representation of the MJO in the Slingo et al. comparison, being one of about three models² that contained variability closely resembling the observed features of the oscillation. In fact, a more rigorous comparison of the intraseasonal variability in the GLA and U.K. Meteorological Office (UKMO) models by Sperber et al. (1997) showed that of the two models, the GLA model tended to produce a better representation of the eastward propagation of convection and its associated cyclonic and anticyclonic circulation anomalies. Slingo et al. also indicate that neither the horizontal resolution nor the numerics (finite difference vs spectral) of the models compared seemed to play a significant role in determining a model’s ability to simulate MJO activity. However, a model’s simulation capability tended to be improved if a convective parameterization was used that did not involve a closure on moisture convergence, for example, Arakawa–Schubert. This was especially true in cases where the mean monthly tropical rain rate was found to increase with SST at a rate equal to, or greater than, that found in the observations.³

Two 10-yr simulations were performed. The first simulation employs specified annual cycle SSTs for the ocean surface boundary condition, and is referred to as the control run (CTL). The second employs a highly idealized, fixed-depth mixed layer model to compute prognostic SST anomalies that are coupled to the atmospheric model. This experiment is referred to as the coupled run (CPL). It is similar in design to that described by Flatau et al. (1997) but employs a slightly more realistic mixed layer formulation and a significantly more realistic atmospheric model and surface energy budget. The model SST equation is

$$\frac{dT'}{dt} = \frac{F'}{\rho C_p H} - \gamma T', \quad (1)$$

where T' is the SST anomaly, F' is the net surface flux anomaly, H is a fixed mixed layer depth, γ is a damping factor, ρ is density, and C_p is specific heat. The slab model is only applied equatorward of 24° , with a linear weighting of 1.0–0.0 between 12° and 24° , respectively. Thus poleward of 24° , there is no SST anomaly in effect and equatorward of 12° , the slab ocean mixed layer is fully active. The net surface flux climatology (12-month annual cycle) used to compute the flux anomalies in the CPL simulation is taken from the CTL simulation. The damping term is meant to keep the model climatologies relatively close and to account for neglected terms (i.e., ocean advection and mixing). In the simulations presented here, γ is set to $(50 \text{ days})^{-1}$. This value ensures that between oscillations the SST comes close to re-

² The three models were the GLA, NCAR Community Climate Model (version 2), and UKMO models.

³ Based on linear regression and satellite-derived estimates of precipitation for the observations (Spencer 1993); see Slingo et al. (1996) for details.

setting itself back to climatology before the next MJO event occurs. This seems appropriate given that the decorrelation scale of tropical intraseasonal behavior is about 50 days, and thus one event tends to have little correlation with the next (Hendon and Salby 1994). The mixed layer depth is taken to be 50 m. Both H and γ were set relatively conservatively in order that the SST anomalies only represent a modest perturbation.

Keeping the SST perturbations small helps ensure that the background climates of the two simulations remain the same and thus any resulting changes in the MJO characteristics between the two simulations can more readily be attributed to the systematic fluctuations in SST associated with the MJO rather than due to changes in the climatological circulation. The sensitivity of the MJO to the climatological state (e.g., Lau and Shen 1988; Wang and Rui 1990b; Li and Wang 1994; Salby and Hendon 1994) is one of the main reasons we undertook the above model setup. Unquestionably coupled ocean–atmosphere models are the ultimate tool for studying the interaction between the MJO and SST. However, at this juncture, jumping to compare simulations of SST-forced GCM runs to their associated fully coupled ocean–atmosphere counterparts produces the following problem. No coupled models to date have a coupled climatology sufficiently close to their forced climatology to offer results that could be used to discriminate the interactive-SST effects alone on the MJO. For example, we know the MJO has pronounced seasonality. We also know that the differences between the observed tropical climatology and that from most, if not all, coupled models is at least as great as the differences one might find between one season and the next in the observations. Thus the differences in the MJO between a fixed-SST and fully coupled simulation will likely be overwhelmed by the differences in the climatology (see summary for further discussion). Moreover, we believe that mixed layer processes are more important in the MJO–SST coupling than dynamic processes simply by virtue of their relative importance in the Indian and western Pacific Oceans where the MJO is most prevalent. With these aspects in mind, we believe the simplified SST coupling undertaken here is a good initial step toward trying to assess the effects of an interactive SST on the MJO without bringing in too many confounding factors.

3. Results

a. Climatologies

Figure 1 shows the 10-yr means of 200-mb velocity potential (VP), precipitation, 200-mb zonal wind and surface zonal wind from the CTL simulation and from observations. In the case of the precipitation, the values come from eight years of Global Precipitation Climatology Project (GPCP; Huffman et al. 1997); otherwise the data are from the National Centers for Environ-

mental Prediction–National Center for Atmospheric Research (NCEP–NCAR) (Kalnay et al. 1996) Reanalysis for the period 1973–92. In general these figures indicate that the model captures the salient features of the mean climate. The overall structure of the 200-mb VP is nearly identical to the reanalysis, although the convergence maximum over Africa and South America is about 25% weaker. The structure of the precipitation field is captured extremely well, except for the warm pool region, where the magnitude is about 20% greater than the GPCP values. The model and reanalyzed 200-mb zonal winds show excellent agreement in the Northern Hemisphere and fair agreement in the other regions. While the character of the upper-level winds in the Tropics is generally the same, there is a westerly bias of about 10 m s^{-1} in the model compared to the reanalysis. This could be a reflection of the different mean phases of the biennial oscillation in the two long-term means or possibly due to the fact that the model simulation does not contain any ENSO variability. A comparison of the surface zonal wind shows remarkably good agreement between the model and reanalysis. These maps and comparisons help to illustrate that the model is fairly proficient at representing the climate of the atmosphere and thus a useful tool for investigating the climatological characteristics of the MJO.

Figure 2 shows the differences in the long-term mean SST, precipitation, 200-mb VP, and surface zonal wind between the CPL and CTL simulations. These figures illustrate the degree the model climate has changed due to the inclusion of the mixed layer coupling. Figure 2a shows the changes to the model surface temperature. As expected, the model SST field shows very little change due to the relatively strong damping applied in the prognostic SST anomaly equation. This implies that the background climatological SST field is the same for both the CTL and CPL simulations, and thus the differences between the simulations with respect to the MJO are not associated with mean SST changes. Systematic changes in the surface temperature over land do exist, however, although the magnitudes are all less than 1°C . The largest of these changes occurs over the Northern Hemisphere continents, with North America cooling by about 1° and central Asia warming by a similar amount. It is not clear whether these changes over land move the model more or less in agreement with observations (not shown) since the very coarse orography of the model ($4^\circ \times 5^\circ$) renders large-scale comparisons with observed temperature climatologies somewhat meaningless.

Figure 2b shows the changes in the long-term mean rain rate between the CTL and CPL simulations. In general, precipitation increases (10%–20%) in the equatorial regions of the Eastern Hemisphere and decreases (10%–30%) over most of the subtropics. Interestingly, there is virtually no change in the zonally averaged rain rate (not shown) and thus much of the differences illustrated imply only a reorganization of the convection.

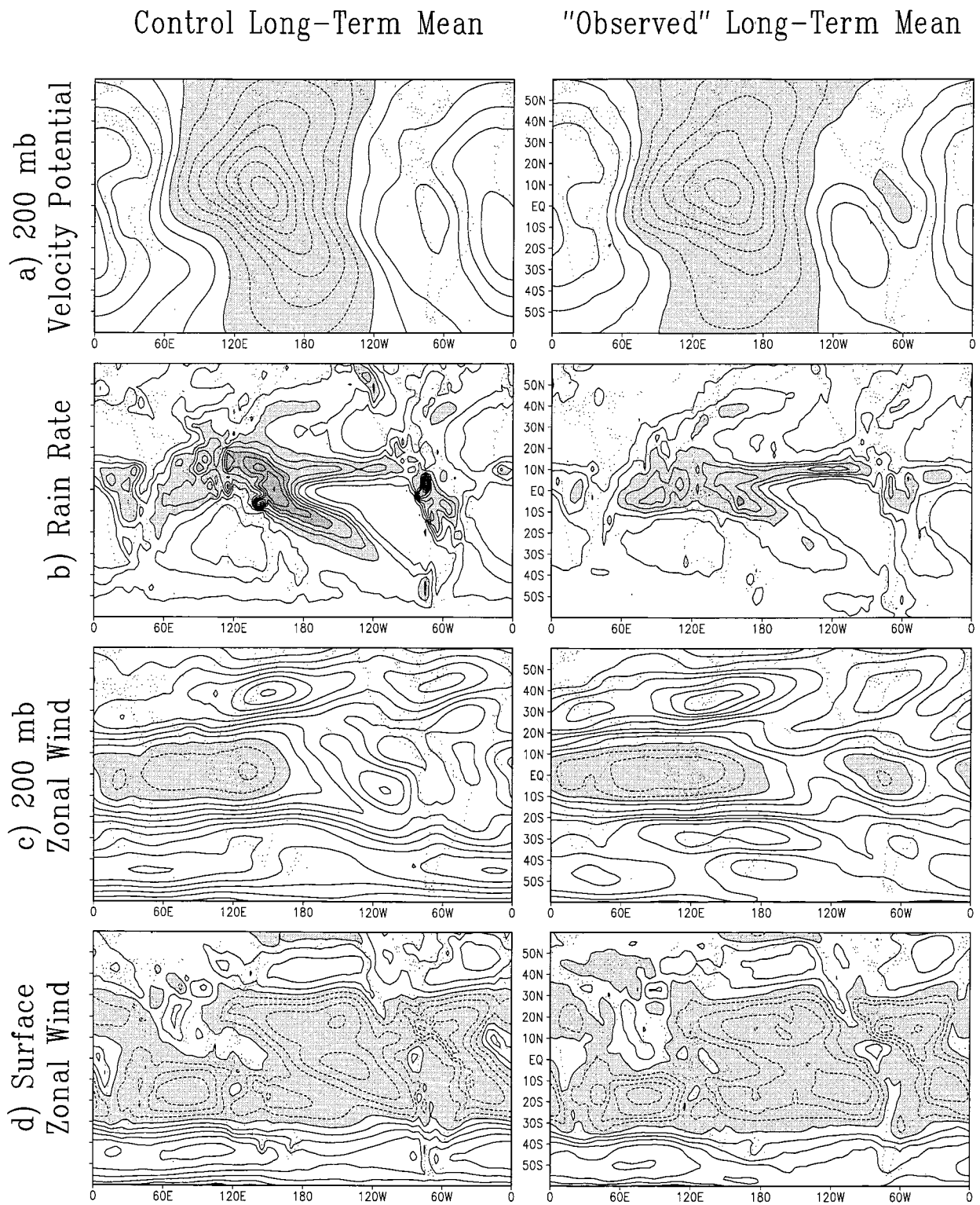


FIG. 1. Long-term means of (a) 200-mb velocity potential, (b) rain rate, (c) 200-mb zonal wind, and (d) surface zonal wind from the control (CTL; left panels) simulation and from observations (right panels). The model fields are 10-yr means. The observed precipitation is from the Global Precipitation Climatology Project from the period July 1987 to June 1996. The other observed fields are from the NCEP–NCAR (Kalnay et al. 1996) Reanalysis for the period 1973–92. Contour intervals are (a) $2 \times 10^6 \text{ m}^2 \text{ s}^{-1}$, (b) 1.5 mm day^{-1} , (c) 5 m s^{-1} , and (d) 2 m s^{-1} . Negative values are shaded except for the rain rate where values over 4.5 mm day^{-1} are shaded.

CPL-CTL Long-Term Mean

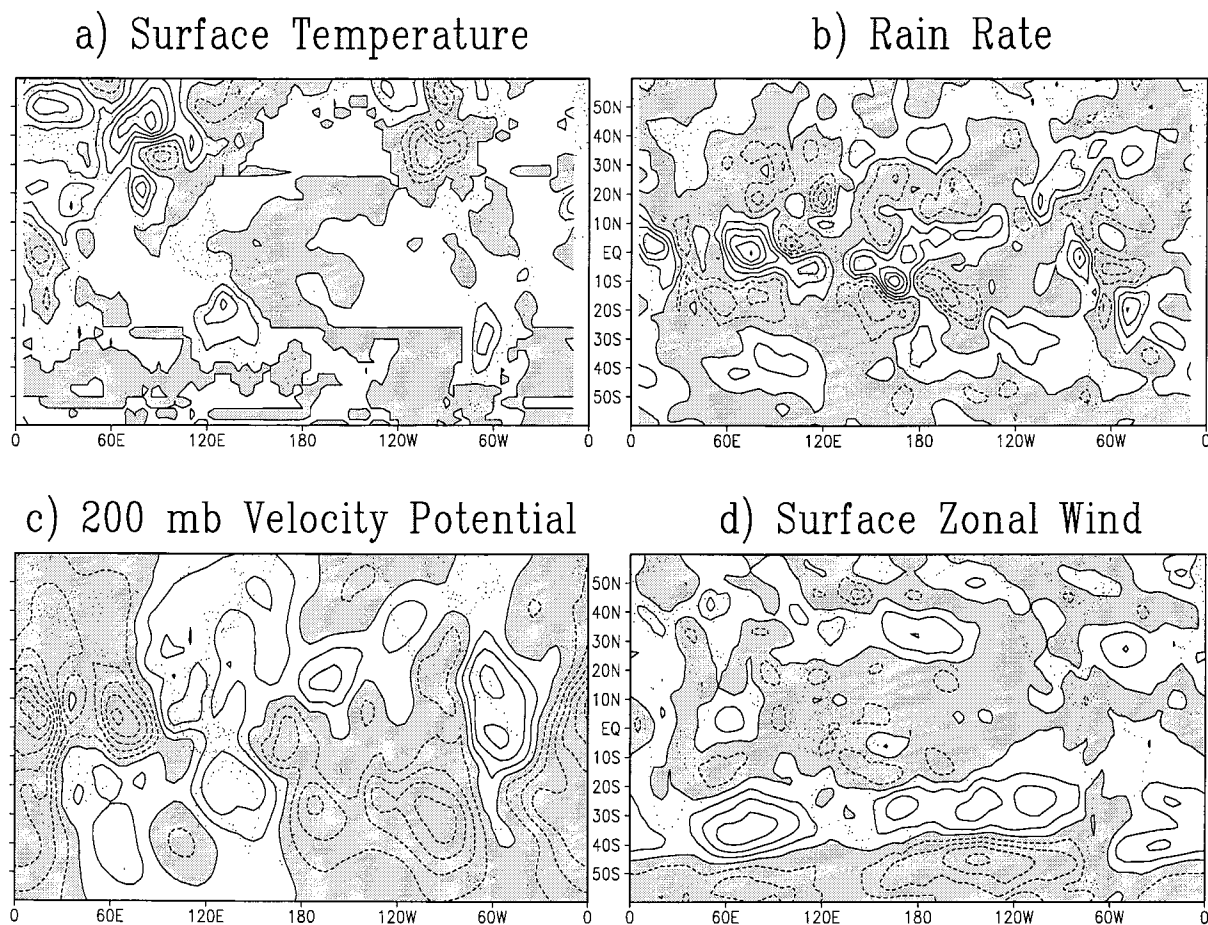


FIG. 2. (left panels) Differences in the long-term means of (a) SST, (b) precipitation, (c) 200-mb velocity potential, and (d) surface zonal wind between the coupled and control (CPL-CTL) simulations. Contour intervals are (a) 0.2°C , (b) 0.2 mm day^{-1} , (c) $0.1 \times 10^6 \text{ m}^2 \text{ s}^{-1}$, and (d) 0.3 m s^{-1} . Negative values are shaded.

Figure 2c shows the changes to the 200-mb VP. In most cases, the changes here mimic those associated with the precipitation but are weaker in terms of relative changes. Over equatorial Africa, the Indian Ocean, and the western Pacific Ocean, there is an increase ($<10\%$) in the upper-level divergence, while over the subtropical southern Indian Ocean, the North Pacific, and northern South America, the opposite occurs. Figure 2d shows the changes in the surface zonal wind. In most cases, the changes are very small. The Southern Hemisphere subtropics and midlatitude ocean regions show systematic changes of the order of 0.5 m s^{-1} ($<10\%$) and the tropical warm pool regions become slightly more easterly (0.25 m s^{-1}). The maps in Fig. 2 are meant to illustrate that the introduction of the tropical ocean mixed layer coupling had a fairly weak impact on the long-term mean model climate, and therefore the changes

in the characteristics of the MJO simulation are not likely the result of changes to the background climate.

b. MJO composites

Figure 3 shows time-longitude plots of the daily average, equatorial (4°N – 4°S), 20- to 100-day bandpassed 200-mb VP for a selected 3-yr period of the two 10-yr simulations.⁴ The $-8 \times 10^6 \text{ m}^2 \text{ s}^{-1}$ contour is filled in order to highlight the stronger MJO events (contour interval is $4 \times 10^6 \text{ m}^2 \text{ s}^{-1}$). Examination of the plot for the CTL simulation shows that the MJO variability as-

⁴ The bandpass filter is constructed from the same 20- and 100-day 100-point Lanczos filters used by, and illustrated in, Slingo et al. (1996).

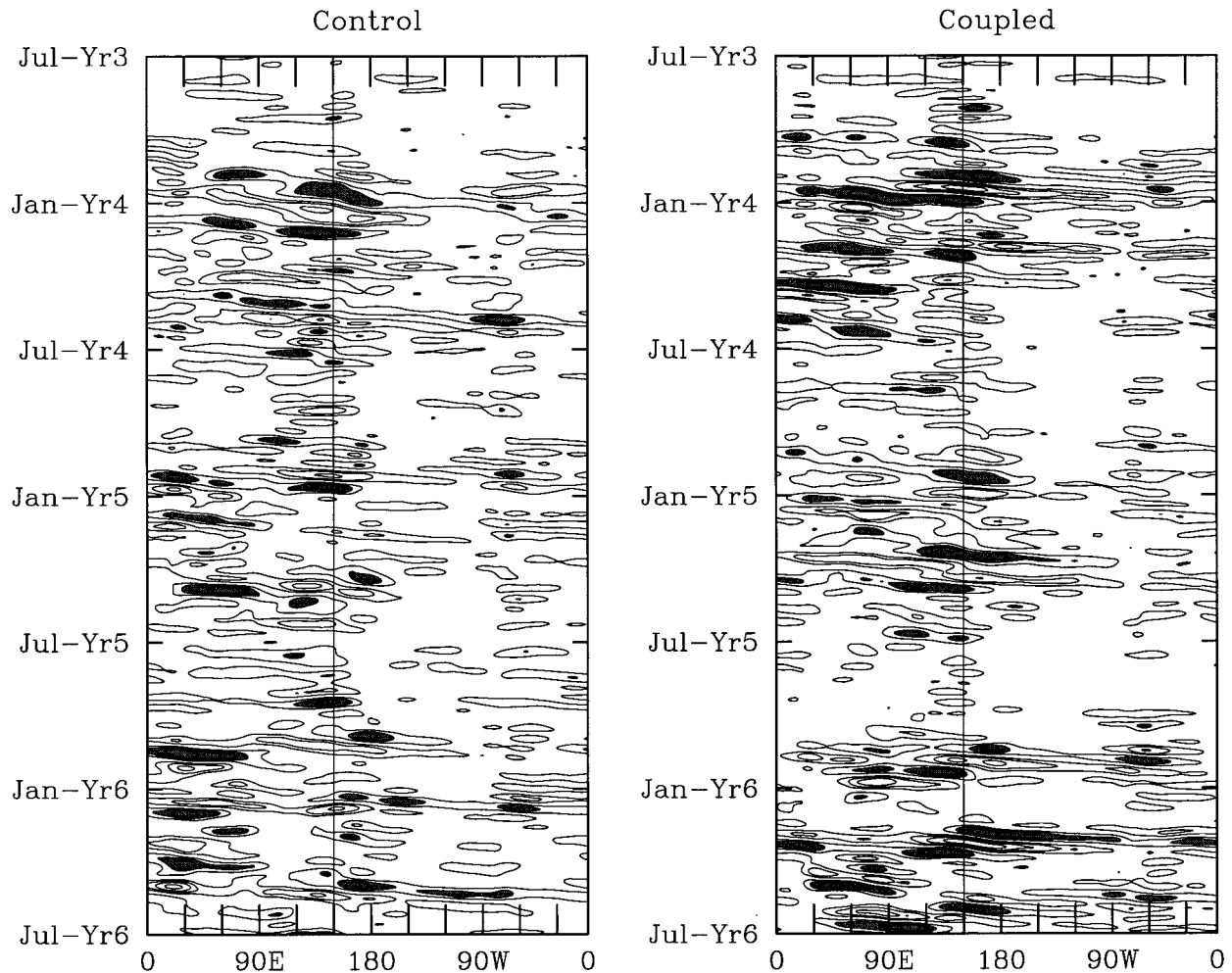


FIG. 3. Time-longitude diagrams of the equatorial (4°N – 4°S) 20–100-day bandpassed 200-mb velocity potential for a selected 3-yr period of the CTL (left) and CPL (right) simulations. The $-8 \times 10^6 \text{ m}^2 \text{ s}^{-1}$ contour is filled. The contour interval is $4 \times 10^6 \text{ m}^2 \text{ s}^{-1}$. The vertical line denotes the 150°E longitude line.

sociated with these stronger events is mostly located in the Eastern Hemisphere with about one “event” per year showing up over South America. The overall character of the time-longitude plot for the CPL simulation is very similar to that for the CTL simulation. However, there appears to be slightly greater variability associated with the strong events, particularly in the first and last years shown, and there also appears to be more events that remain stronger and more coherent over a longer distance. For example, there are eight events that remain coherent over 60° in longitude with an anomaly strength of $-8 \times 10^6 \text{ m}^2 \text{ s}^{-1}$ in the CTL simulation and 12 in the CPL simulation. Further, there is a more obvious seasonality in the CPL simulation, with the MJO events being more strongly confined to the northern winter months.

In an effort to characterize the differences in the MJO simulation in more detail we have produced composite MJO events from each experiment using the 20–100-

day bandpassed data. Figure 4 shows time-longitude diagrams of the 200-mb VP and zonal wind for these composite events. As with Fig. 3, the composites are based on daily mean data averaged in latitude between 4°N and 4°S . In each case and for each variable discussed, the composite includes only events that had a 200-mb VP anomaly falling below $-10 \times 10^6 \text{ m}^2 \text{ s}^{-1}$ at a longitude of 150°E (indicated by the vertical line; see also Fig. 3). This longitude was chosen due to its close proximity to the TOGA COARE region, which encountered a number of MJO events during the Intensive Observation Period (IOP) that have since been, and will continue to be, analyzed in great detail (e.g., Nakazawa 1995; Weller and Anderson 1996; Waliser et al. 1996; Lin and Johnson 1996; Lau and Sui 1997). Readily apparent is the increased overall strength of the oscillation in both fields of the CPL experiment versus the CTL experiment, particularly in the VP field. This increase in MJO strength is also reflected in the number

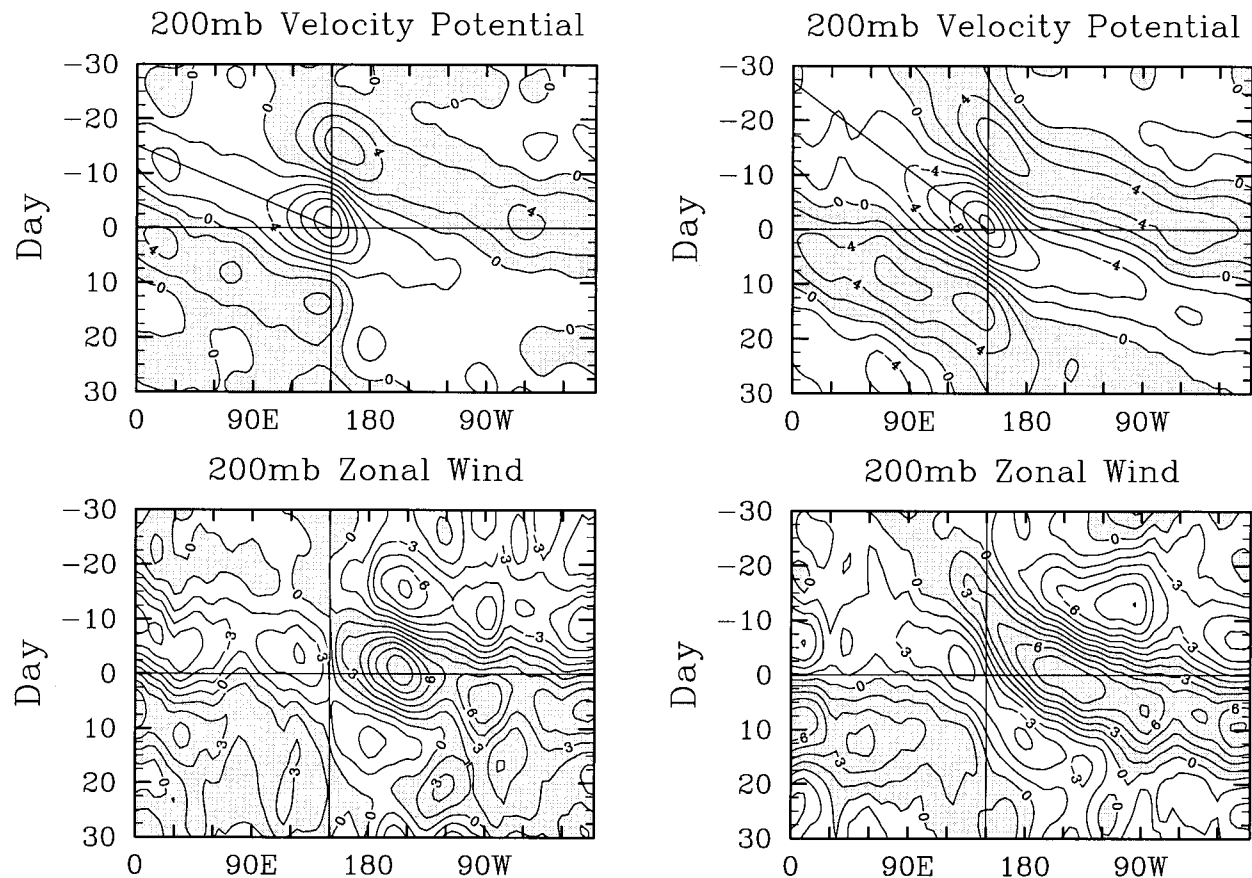


FIG. 4. Time-longitude composites of the 20–100-day bandpassed 20-mb velocity potential and zonal wind for a composite MJO event from the CTL (left) and CPL (right) simulations. The data are based on daily means averaged in latitude between 4°N and 4°S. In each case and for both variables, the composite includes only events that had a 200-mb VP anomaly falling below $-10 \times 10^6 \text{ m}^2 \text{ s}^{-1}$ at a longitude of 150°E (indicated by the vertical line). There are 15 (23) events in the CTL (CPL) composite. Contour intervals for VP and wind are $-2 \times 10^6 \text{ m}^2 \text{ s}^{-1}$ and 1.5 m s^{-1} , and positive anomalies are shaded in each case.

of events that meet the VP compositing criteria. Based on the above threshold, the CPL simulation had 23 events versus 15 for the CTL simulation.

Figure 5 shows the dependence of this increased number of MJO events (as defined above) in the CPL simulation versus the VP threshold and selection longitude. The top contour plot shows the number of events that meet the VP threshold (left axis) as a function of the selection longitude (lower axis) for the CTL simulation. For example, the selection longitude for the composites in Fig. 4 is 150°E and the VP threshold is $-10 \times 10^6 \text{ m}^2 \text{ s}^{-1}$, and thus the number of MJO events is shown to be 15, as indicated above. As expected, there is an Eastern Hemisphere preference for the occurrence of the MJO and a diminished MJO frequency in the central and eastern equatorial Pacific. Figure 5b shows the difference between the same plot for the CPL simulation (not shown) and Fig. 5a, and thus the increase in the number of identifiable events associated with a given VP threshold for each longitude. Note that for VP thresholds between -6 and $-10 \times 10^6 \text{ m}^2 \text{ s}^{-1}$, there is an increase of about four to eight events over most

longitudes, or about 0.5–1 event per year. Figure 5c shows the relative increase in the number of events for the CPL simulation versus VP threshold and selection longitude. Evident is the larger relative enhancement for the strongest events, especially over warm pool regions of the Indian and Pacific Oceans and over the eastern-central Pacific.

From the three years of model output plotted in Fig. 3, it appears that there was a marked enhancement in the occurrence of equatorially propagating MJO events in the northern winter and spring seasons. Observational studies indicate that equatorial disturbances strongly favor the October–May period, and in particular from December onward (e.g., Salby and Hendon 1994, see their Fig. 7; Wang and Rui 1990b). The model comparison study by Slingo et al. (1996) remarked on the poor representation of the observed MJO seasonality in nearly all of the models they analyzed. For this reason, it is worth presenting a seasonal breakdown of the number of the events for the CTL and CPL simulations (15 and 23, respectively) for the compositing longitude chosen (150°E). These data are shown in Fig. 6 and illustrate

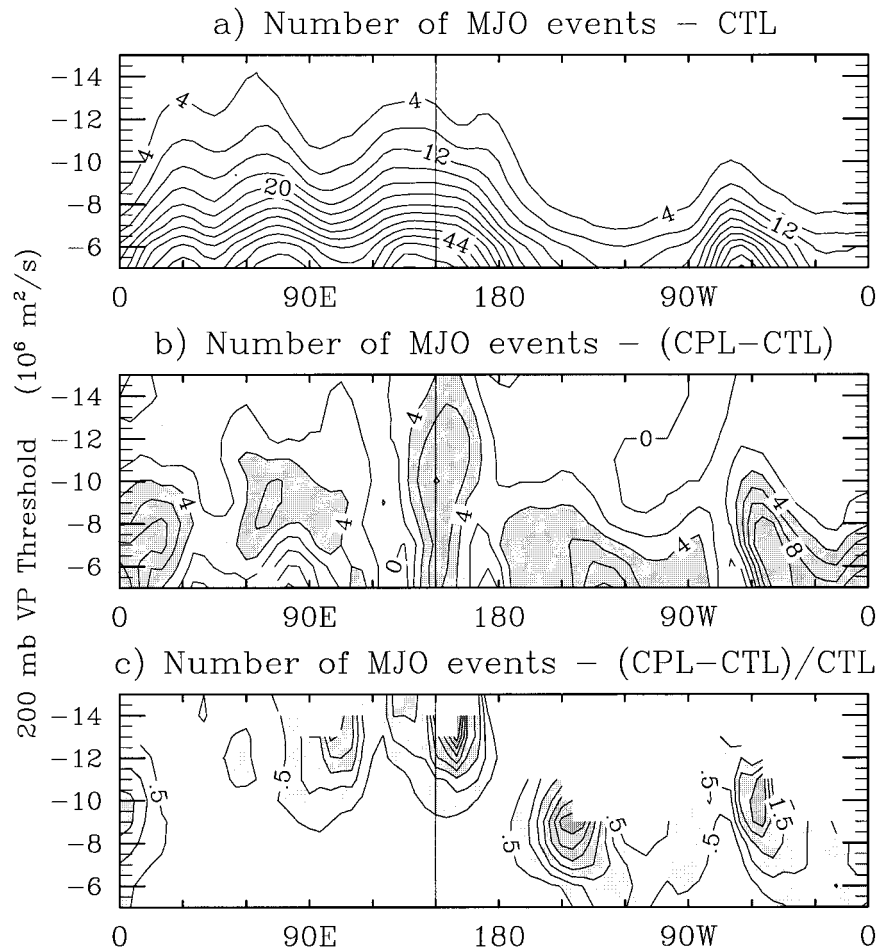


FIG. 5. (a) Number of MJO events that meet the specified VP anomaly threshold criteria (left axis) as a function of longitude (lower axis) for the CTL simulation. (b) As in (a), except for the difference in the number of events between the CPL and CTL simulations. (c) As in (b), except for the relative increase in events. Contour intervals are (a) 4, (b) 2, and (c) 0.5.

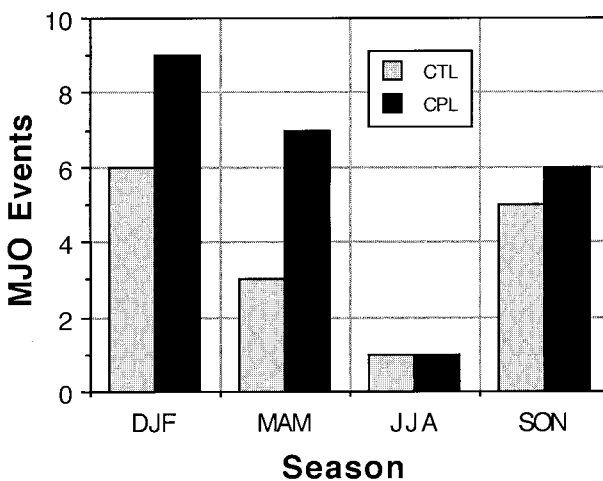


FIG. 6. Seasonal breakdown in the number of events making up the MJO composite events shown in Fig. 4 from the CTL (gray; 15 total) and CPL simulations (black; 23 total).

that the CPL simulation had a 50% increase in the number of events from December to February (six to nine), a 133% increase from March to May (three to seven), a 0% increase from June to August (one to one), and a 20% increase from September to October (five to six). From these numbers, it is apparent that the CPL simulation does indeed show a more striking seasonality, with a marked increase during the seasons favoring equatorial intraseasonal variability, and little or no increase during the seasons when the equatorial intraseasonal signal is weakest.

The composites in Fig. 4 also show that there is a more obvious change of phase speed in the 200-mb VP between the Eastern and Western Hemispheres in the CPL simulation compared to the CTL simulation, with the main factor being a decrease in phase speed in the Eastern Hemisphere from about 13 m s^{-1} for the CTL simulation to about 7 m s^{-1} for the CPL simulation (denoted by the two diagonal lines). Note that this decrease in phase speed is evident in the subsidence pe-

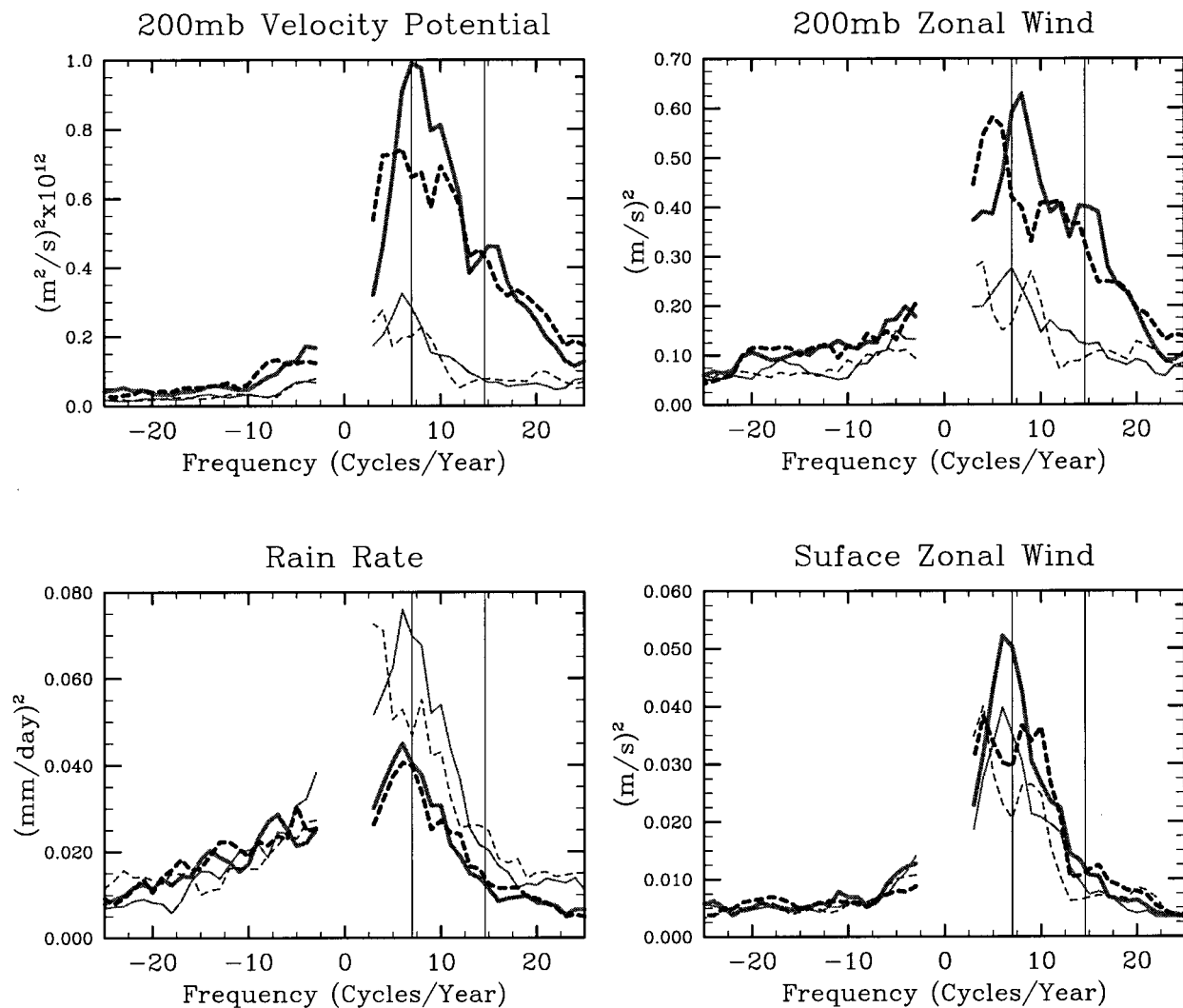


FIG. 7. Wavenumber-one (thick) and -two (thin) frequency spectra of the equatorial (4°N and 4°S) 200-mb velocity potential (upper left), 200-mb zonal wind (upper right), rain rate (lower left), and surface zonal wind (lower right) from the CTL (dotted) and CPL (solid) simulations. Vertical lines denote 55- and 25-day periods. See text for method of computation.

riod/region prior to the event but not very evident in the subsidence period/region after the event. This decrease in phase speed associated ocean coupling was found in the coupled theoretical model of Wang and Xie (1998). Their model indicates that the feedback from wind-entrainment/evaporation (somewhat analogous here to the net flux feedback on our slab ocean; see sections 3d,e) were largely responsible for slowing and destabilizing what would otherwise be a neutral moist Kelvin wave in a case without SST coupling. In their analysis, slow disturbances with low wavenumbers were preferentially destabilized, since they would be the most effective at modifying and interacting with SST. Another striking difference in these two sets of composites is the greater continuity and organization of the wavenumber-one features in these two variables across all longitudes in the CPL versus the CTL simulation. This may reflect

a narrow selection of frequency and wavenumbers that make up the MJO disturbances in the CPL simulation.

c. Intraseasonal variance structure

Figure 7 displays the wavenumber-one and wavenumber-two frequency spectra for the two simulations for 200-mb VP, 200-mb zonal wind, rain rate, and surface zonal wind. These spectra were computed for each year of the anomaly data (about the annual cycle) and then the ensemble average of the 10 yr computed. Thus variability with periods greater than the about 180 days (i.e., semiannual cycle) has been removed and the corresponding values in the plots set to zero. Consistent with the results in Figs. 4 and 5 is an increase in the peak power of the wavenumber-one VP of about 40% in the CPL simulation. Also evident is an increase in

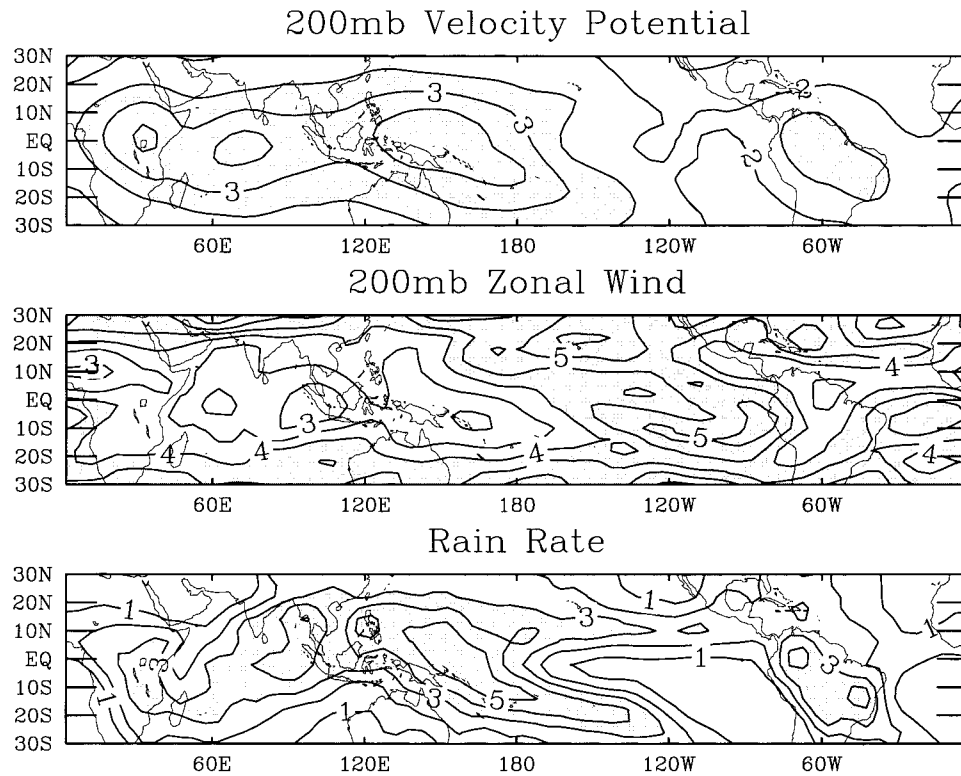


FIG. 8. Standard deviations of 200-mb VP, 200-mb zonal wind, and rain rate associated with variability between 25 and 65 days for the CTL simulation; contour intervals are $0.5 \times 10^6 \text{ m}^2 \text{ s}^{-1}$, 0.5 m s^{-1} , 1.0 mm day^{-1} .

peak power in the surface zonal wind spectra of about 45%. In both these cases, the increase in power at around 50 days is significant at a 90% confidence level.⁵ Rain rate is known to contain most variability in wavenumber two, and again the CPL simulation shows a similar size increase over the CTL simulation in wavenumber-two power at around 50 days. Note also that in most cases of the variables shown there is a reorganization of the wavenumber-one and/or -two variance, with a tendency for more power at the primary timescales evident in the observations (i.e., at 50–60 days and about 25 days; see Slingo et al. 1996; Hayashi and Golder 1993); these two timescales are highlighted by two vertical lines.

To illustrate the spatial dependence of the changes evident in the power spectra between the two simulations, Fig. 8 shows the standard deviations of 200-mb VP, 200-mb zonal wind, and rain rate associated with

variability between 25 and 65 days⁶ for the CTL simulation. The spatial structure of the standard deviation in rainfall indicates that most of the 25–65-day variability is confined to the Eastern Hemisphere, consistent with observed results using either outgoing longwave radiation or highly reflective clouds as a proxy for tropical rainfall (e.g., Lau and Chan 1988; Waliser et al. 1993). A similar structure is depicted in the VP field with an almost inverse structure depicted for the 200-mb zonal wind. In each case, these bandpassed standard deviation fields have some resemblance to their mean tropical structures shown in Fig. 1. Thus the variability in these fields, in this frequency range, tends to be largest where the mean values are largest and vice versa.

Figure 9 shows the changes to the above CTL standard deviation maps associated with the CPL simulation, as well as the 25–65-day variability in model SST. These standard deviation difference maps (CPL–CTL) indicate that the enhanced MJO variability in the CPL simulation shows up principally in the western Pacific, portions of the Indian Ocean, and over much of South America. The 200-mb VP in particular shows the most

⁵ The number of degrees of freedom used was 60. This value was derived from the fact that the spectra in Fig. 7 were the average of the spectra from 10 1-yr long records. This gives 20 degrees of freedom at each point. In addition, the spectra were smoothed with a three-point box filter, yielding a value of 60. Moreover, dividing the record length (3650 days) by the 50-day timescale of interest gives a rough estimate (≈ 70) of the upper limit on the number of degrees of freedom.

⁶ In this case, 25- and 65-day 100-point Lanczos filters were applied to obtain the bandpassed data.

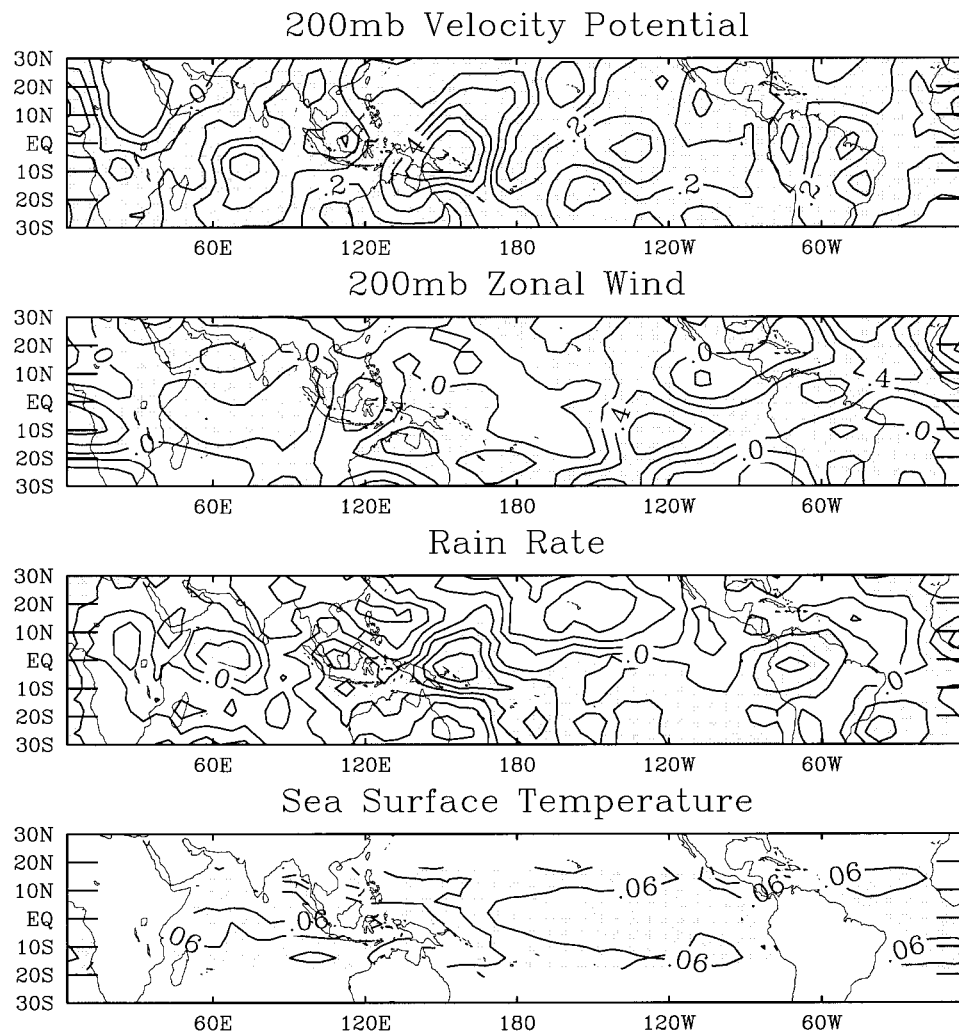


FIG. 9. Differences between the CPL and CTL (CPL–CTL) standard deviations of 200-mb VP, 200-mb zonal wind, rain rate, and SST associated with variability between 25 and 65 days; contour intervals are $0.1 \times 10^6 \text{ m}^2 \text{ s}^{-1}$, 0.2 m s^{-1} , 0.1 mm day^{-1} , and 0.03°C .

widespread increases, which are on the order of 10% or more. The 200-mb zonal wind exhibits increases throughout most of the Western Hemisphere and into the Indian Ocean region. Rainfall variability in the 25–65-day band is enhanced by about 10% over the maritime continent, the western Indian Ocean, and western South America. This latter variability may be a by-product of orographic forcing associated with the South American land mass and the more robust MJO VP signal in the CPL simulation, which emanates farther eastward from the western Pacific, well past the date line (see Fig. 4). Note also that these changes in the bandpassed rainfall and 200-mb VP variability closely mimic the changes between the CPL and CTL long-term means (Fig. 2). The SST variability associated with the model mixed layer shows highest variance in the western Pacific, where the MJO variability and the enhancements to it are most evident. Here the bandpassed standard

deviations are on the order of 0.1°C with the rest of the tropical ocean regions exhibiting values of about 0.05°C . In addition to the added variability in SST over the tropical ocean (associated with the active domain of the model mixed layer), changes in surface temperature variability over land also occur (not shown). The variability increased modestly over the Maritime Continent by about 0.1°C , decreased over central Africa by about 0.2°C (see Fig. 10 and discussion below), and decreased a similar amount over most of the subtropical land masses, except in the area of the Sahara, where it showed a slight increase.

d. SST variations

The connection between the MJO and the SST variability described above is more easily illustrated by the surface temperature composites shown in Fig. 10, which

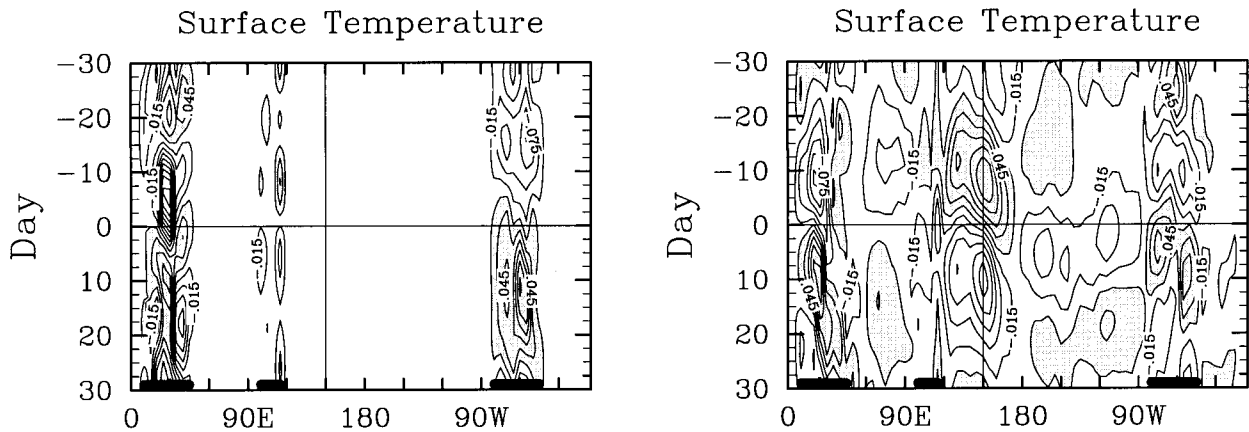


FIG. 10. Same as Fig. 4, except surface temperature. Contour interval is 0.03°C . Note that values at longitudes that contain land masses, indicated by the thick bars at the bottom of the plot, have been divided by 4.0. This was done so that the variability over ocean and land regions could be presented together on a single plot.

are based on the same procedure that produced composites in Fig. 4. Note that these composites contain both land and ocean temperature fluctuations, with the former being considerably larger due to the much smaller heat capacity of the land surface versus the 50-m ocean mixed layer. The longitudes containing land grid points are indicated at the bottom of the plots by thick bars. In order to present the evolution of both on the same plot, the values associated with land temperature fluctuations were divided by 4. As expected, the CTL SST variations are zero, while the CPL SST anomalies show evidence of a heating-cooling signature in quadrature with the propagation of the 200-mb VP anomaly (Fig. 4), with warm SST ahead of the convection and cool SST behind it. In addition to the SST fluctuations in the CPL simulation, both simulations show significant variability ($\pm 0.5^{\circ}$ – 1.0°C ; see figure caption) over land areas. The main differences between the CPL and the CTL simulations consist of a frequency doubling of the variability (~ 60 to ~ 30 days) over South America and a frequency halving (~ 30 to ~ 60 days) over Africa. At present we do not consider these land temperature changes to be important with respect to this study's objectives or conclusions; however, it would be interesting investigate their origin(s) and determine which of the model relationships (CTL or CPL) is more consistent with observations.

The results concerning the SST changes, namely, the structure and magnitude of the SST in the CPL composite, come fairly close to mimicking the observed MJO–SST behavior. Figure 11 shows composites similar to those discussed above except they are based on pentads of observed OLR and SST⁷ from 1985 to 1994 taken from Jones et al. (1998). In this case, the data are

bandpassed in the same manner as for the model data; however, instead of compositing the events based on velocity potential, here composites include all events in which the bandpassed OLR anomaly fell below -27 W m^{-2} . This threshold was chosen to give about the same number of events as in the CPL model MJO composite. For comparison purposes, the OLR evolution associated with the CPL composite MJO (i.e., Fig. 4) is also shown. A comparison of the CPL SST composite of Fig. 10 and the observed SST composite of Fig. 11 shows that the overall magnitude of the SST variation is roughly in line with observations, and the phase of the SST anomalies with respect to the convection are also in good agreement, especially in the Indian Ocean and warm pool regions. The reason for the poorer agreement in the eastern Pacific is likely due to the important influence of ocean dynamics (e.g., Legeckis 1977; McPhaden 1996), which is not accounted for in the slab ocean mixed layer model. With respect to the good agreement evident in the Eastern Hemisphere SST, it should be noted that some observed MJO events (e.g., the TOGA COARE period) are associated with much larger changes in SST (e.g., Weller and Anderson 1996), and it is possible that the SST analysis underestimates the SST variability in this band due to the prevalence of clouds in this region and the analysis's dependence on satellite data. Furthermore, for the reasons outlined in section 2, the model mixed layer is also likely to be underestimating the magnitude of the intraseasonal SST variability.

e. Surface and PBL processes

Associated with the above changes in SST, and the dynamical changes evident in Fig. 4, are low-level moisture changes. Figure 12 shows composites analogous to those in Fig. 4, except for planetary boundary layer

⁷ These SST data are from European Centre for Medium-Range Forecasts analyses.

(PBL)⁸ specific humidity. Consistent with much of the above discussion, this figure shows that the MJO signal in the CPL versus CTL simulation is more organized and coherent as it propagates eastward from the Indian to the Pacific Ocean, has a slower phase speed in this region, and shows consistently larger variations between moist and dry periods/regions. The composite also shows that the maximum PBL specific humidity anomaly lags the maximum SST anomaly by about 3–4 days and leads the minimum 200-mb VP anomaly by about 4–5 days.

The profiles shown in Fig. 13 provide some initial clues as to the possible reason for the enhanced MJO variability in the case with the interactive SSTs versus the case with fixed SSTs. These profiles are longitudinal averages, from 145° to 155°E, of the data in the time–longitude MJO composites discussed above. For example, the profiles shown in Fig. 13h are taken from the 200-mb zonal velocity time–longitude composites shown at the bottom of Fig. 4 (i.e., an average of the model grid points along, and to either side of, the vertical line). The thin line in each profile is taken from the CTL MJO composite and the thick line is taken from the CPL composite. Note that day 0 is when the 200-mb VP reaches its minimum for the composite event. Figures 13a and 13b show the MJO's influence on the two dominant surface heat flux terms.⁹ For each simulation, the negative latent heat flux anomaly is largest (-30 W m^{-2}) about 13 days before the passage of the MJO convection center while the positive latent heat flux anomaly is largest ($+25\text{--}30 \text{ W m}^{-2}$) about 3 days after its passage. This is consistent with a number of observational studies, including Jones and Weare (1996), Lau and Sui (1997), Jones et al. (1998), and Hendon and Glick (1997); it is, however, at odds with the evaporation–wind feedback hypothesis (Neelin et al. 1987; Emanuel 1987). Note that the CPL simulation shows about a 30%–40% enhancement in the positive latent heat flux anomaly that occurs after the passage of the MJO, with little or no change before. As expected, the surface shortwave flux anomalies show enhanced downwelling shortwave flux ($12\text{--}18 \text{ W m}^{-2}$) about 20 days ahead and about 12 days behind the convection, with greatly diminished shortwave flux (-30 W m^{-2}) during the passage of the convection. These model-simulated shortwave changes are about 40% larger than those seen in the observed composite of satellite-derived shortwave flux constructed by Jones et al. (1998). Note that the peak modulation of the OLR and rain rate (not shown) occur at approximately the same time as the peak modulation of downwelling shortwave flux, and

thus the peak rainfall precedes the peak VP anomaly by about 3 days.

Given the weak variability in the surface sensible and net longwave flux, the profile for the net surface heat flux shown in Fig. 13c is nearly equal to the sum of the profiles for evaporation and shortwave flux. This net flux profile indicates enhanced surface heating of the order of 35 W m^{-2} about 15 days before the VP minimum, enhanced surface cooling of the order of 50 W m^{-2} during the time the VP is at a minimum (i.e., heavy precipitation period), and then a return to near normal conditions and/or weak surface heating about 10–20 days after the event. Based on the slab mixed layer specifications (i.e., 50-m fixed-depth slab ocean with 50-day damping), this results in about a 0.13°C positive (negative) SST anomaly before (after) the VP minimum, with a quadrature delay relative to the surface net heat flux variations. This enhancement to the SST before the MJO passage is associated with an increase in the PBL specific humidity over that which is seen in the CTL simulation (Fig. 13e). In the CTL simulation, there is a weak positive anomaly in the PBL specific humidity of 0.25 gm kg^{-1} at lag -6 days, or about 3 days before the peak rainfall event. In the CPL simulation, this anomaly has doubled. This enhancement to the PBL moisture anomaly before the event is mimicked in the negative anomaly (i.e., dry phase) that occurs after the event, although the effect is even more dramatic.

Comparing the magnitudes of the enhanced positive PBL humidity and SST anomalies in Fig. 13 (see also Figs. 10 and 12) suggests that the increased humidity does not stem from a local adjustment to the warmer SST. In other words, assuming the PBL in the deep Tropics is typically about 80% moisture saturated with respect to the SST, and given that the mean SST in this region is about 28°C , a 0.1°C change in SST would only lead to about a 0.1 gm kg^{-1} increase in PBL specific humidity. This is only about one-third of the enhancement found in the CPL simulation. In any case, the lack of any associated enhancement in the surface latent heat flux before the convection suggests that even this amount of adjustment did not occur via latent heat flux. The reason behind this increased PBL moisture convergence anomaly is believed to be the critical process underlying the enhancement of the MJO in the CPL simulation, and it will be discussed in more detail in section 4. Examination of Figs. 13e and 13f shows that the enhanced PBL moisture anomaly leading the convection in the CPL simulation is associated with a 25% enhancement in the PBL moisture convergence anomaly. The profiles for rain rate (not shown) are nearly identical to the PBL moisture convergence profiles, but with the anomalies about a factor of 3 larger and a phase lag relative to the PBL moisture convergence of about 2–3 days (or about one to two model grid points to the west). The lower- and upper-level dynamic effects of the enhanced MJO are illustrated in Figs. 13g and 13h, respectively, which shows the considerable strength-

⁸ In this study, the PBL is defined as the lowest three sigma layers, with the middle of the uppermost of these layers having a sigma value equal to 0.92992.

⁹ Modulations to the longwave and sensible heat flux terms are on the order of 5 W m^{-2} .

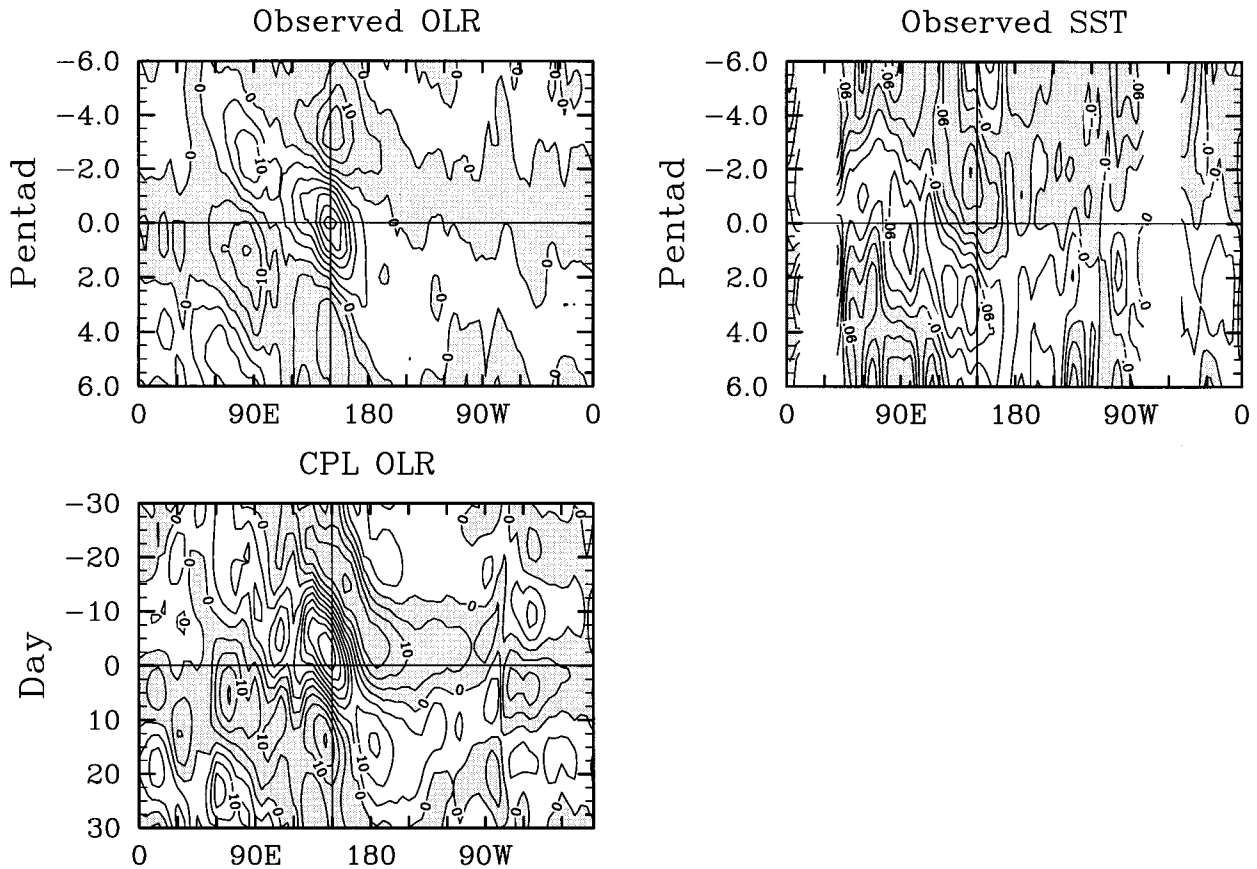


FIG. 11. Same as Fig. 4, except based on pentads of observed OLR and SST from 1985 to 1994. In this case, the data are bandpassed in the same manner as for the model data; however, instead of compositing the events based on velocity potential, here events were included in the composites each time the bandpassed OLR anomaly was less than -27 W m^{-2} ; this gave 22 events (from Jones et al. 1998). Contour intervals for OLR and SST are 5 W m^{-2} and 0.03°C . For comparison purposes, the OLR evolution associated with the CPL MJO composite (i.e., Fig. 4) is also shown.

ening of the surface and 200-mb zonal wind field. It is worth mentioning that the profile of surface latent heat flux strongly resembles the evolution of surface zonal wind. While it is understood that variability in latent heat flux in the warm pool regions is largely driven by

variability in wind speed (e.g., Zhang and McPhaden 1995), it is not obvious why in this case it should be driven by zonal wind alone. Examination of Fig. 1 shows that the longitude that this equatorial composite was produced (150°E) is an area of very weak zonal

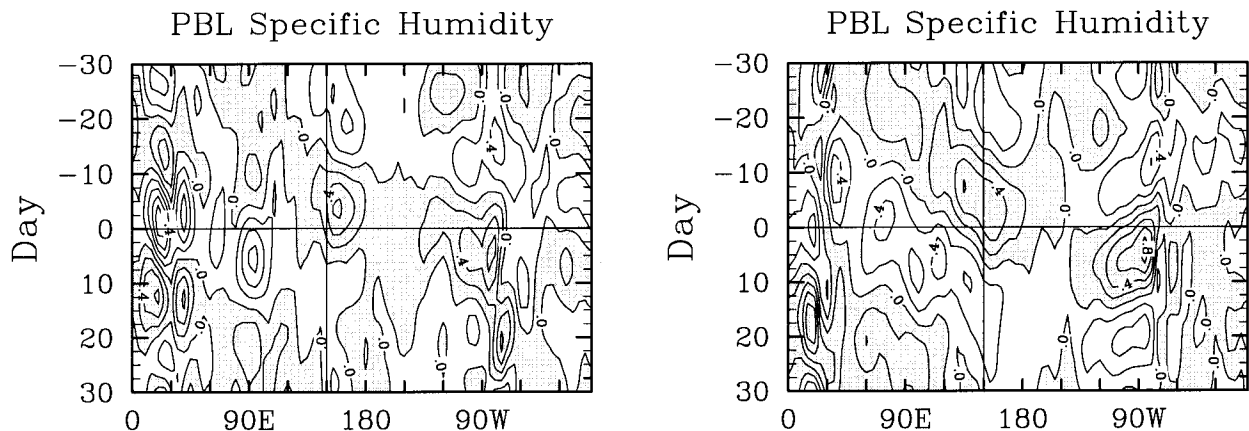


FIG. 12. Same as Fig. 4, except for planetary boundary layer specific humidity ($\sigma = 0.94\text{--}1.0$). Contour interval is 0.2 gm kg^{-1} .

winds. This, along with the fact that the intraseasonal perturbations to the surface meridional velocity (not shown) are about one-fourth the magnitude of those to the zonal velocity, dictates that most of the wind speed, and thus latent heat flux, variability will be determined by the variability in zonal wind.

f. Atmospheric circulation and latent heating

The changes to the dynamics and convection–rainfall described above due to the influence of the interactive SST are also illustrated in Fig. 14, which shows the vertical and zonal velocity (vectors) and latent heating (contours) values associated with the composite MJOs. The left panels show these fields for the CTL composite (e.g., left panels of Fig. 4) at lag -5 days (top) and $+5$ days (bottom). The right panels show the difference between the CPL and CTL composites for these fields at the same two time lags. The CTL composites show a strong baroclinic structure with positive rainfall anomalies (up to $6^{\circ}\text{C day}^{-1}$) extending from about 135° to 165°E , and subsidence occurring to both the east and west of the maximum rainfall. Note that in this phase of the oscillation the surface easterlies to the east of the rainfall are about twice as strong as the anomalous westerlies to the west of it (about 4 vs 2 m s^{-1}). At lag $+5$, the rainfall anomaly has weakened considerably, moved slightly eastward, and is now spread between about 150° and 170°E . In this phase the anomalous westerlies have significantly more strength than the anomalous easterlies.

The difference plots on the right side of Fig. 14 show the enhancements to the MJO circulation associated with the SST feedback. At lag -5 days, there is stronger upward motion and more atmospheric latent heating (up to about $3^{\circ}\text{C day}^{-1}$) west of 150°E , and stronger downward motion to the east. These changes produce asymmetrical changes in the surface fluxes (not shown) with increased (decreased) shortwave flux east (west) of 150°E of about 10 W m^{-2} . On the other hand, latent heat fluxes only show a systematic increase, up to $10\text{--}15\text{ W m}^{-2}$ west of 150°E . At lag $+5$ days, there is stronger upward motion and more atmospheric latent heating (up to about $2^{\circ}\text{C day}^{-1}$) east of 150°E and stronger downward motion to the west. Changes to the shortwave flux associated with the enhanced vertical motions are commensurate with those at lag -5 days, and again the principle change in the latent heat flux is an enhancement that occurs at, or to the west of, the main region of rainfall enhancement. Most of these differences are consistent with the evolution depicted in the time-lag profiles shown in Fig. 13, except that the shortwave flux ahead of the convection in the time-lag profiles showed little or no difference between the coupled and control experiment. Finally, it is worth noting that the two regions of enhanced upward (downward) motion in the lag -5 ($+5$) day composite are over, or in close proximity to, (model) equatorial land masses. This is

consistent with Fig. 9, which shows that the rain rate has increased variance over, and around, land masses in the equatorial maritime region.

To help illustrate the model dynamics that appear to be playing a role in the production of the MJO itself, and subsequently what may be playing a role in the SST-driven enhancement to the MJO, Fig. 15 presents the zonally lagged correlations between the midtropospheric vertical velocity and the vertical velocity at all levels for the CTL simulation (left) along with the difference in this quantity between the CPL and CTL simulations (right). The computations are based on the same CTL and CPL composite data shown in Fig. 14, using the longitude range $100^{\circ}\text{E}\text{--}160^{\circ}\text{W}$ and time lags from -15 to $+15$ days. For each day (i.e., time lag), the vertical velocity at $\sigma = 0.58$ is correlated to the vertical velocity at all sigma levels, allowing the zonal lag to vary between ± 12 model grid points. Then each of these correlations maps (sigma vs zonal lag), 31 in total, are ensemble averaged together. The correlation plot for the CTL simulation (left) illustrates a westward tilt with height, on the order of 1000 km (two model grid points) over the depth of the troposphere, suggesting the presence of wave–CISK in the model (e.g., Lau and Peng 1987; Lau et al. 1988). Analysis of the GLA MJO-related 200- and 850-mb eddy streamfunction by Sperber et al. (1997) also indicated a tropospheric westward tilt with height. In addition, the tilting tends to accentuate in the boundary layer, with the maximum upward vertical motion in the surface layer appearing to lead that at midlevels by about 15° longitude (three grid points). This latter characteristic is consistent with “frictional wave–CISK,” that is, the impact of boundary layer friction on wave–CISK (Wang 1988a; Salby et al. 1994). A similar analysis of a coarse-resolution version of the Geophysical Fluid Dynamics Laboratory GCM revealed a similar characteristic (Lau et al. 1989). It is interesting that this feature was not evident in the GLA MJO analysis by Sperber et al. (1997), either because of their case study approach, which employed a limited amount of data, and/or because their study examined the wind divergence on a single near-surface layer that may be subject to more noise than the vertical velocity as it is an integrated quantity over one or more model layers. The right panel shows that the positive correlation between midlevel and upper- and lower-tropospheric vertical velocity has a slight wider zonal scale with slightly higher correlation values. This reemphasizes the slightly stronger and more coherent MJO found in the CPL versus CTL composite. However, near the surface, the CTL simulation shows a more consistent area of upward vertical motion about $20^{\circ}\text{--}30^{\circ}$ to the east of the region of midlevel rising motion. This area of enhanced low-level convergence can also be inferred from the region of enhanced latent heating and upward motion at 160°E (160°W) in the upper (lower) right panel of Fig. 14. This area of enhanced vertical motion might be interpreted as a strengthening of the frictional

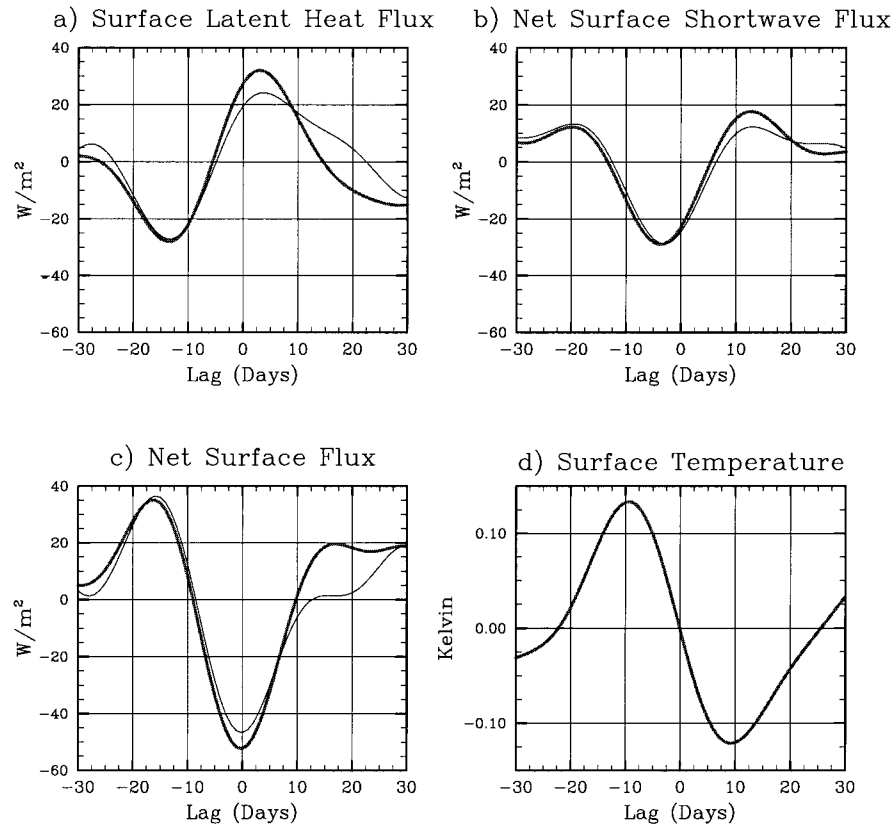


FIG. 13. Profiles taken from CTL (thin) and CPL (thick) composite MJO events. Data are averaged between 145° and 155°E . For example, profiles in (h) are taken from the CTL and CPL 200-mb zonal wind composites in Fig. 4. The profiles are based on data along the vertical line shown in

wave-CISK process in the model. How such an enhancement may occur via the incorporation of an interactive SST feedback is discussed below.

4. Discussion

The previous section illustrates that the CPL simulation generally exhibits a more robust MJO phenomena relative to the CTL simulation. This is evident from the increase in the number of MJO events in the CPL simulation (Fig. 5) and from the strengthened and more coherent character of the CPL versus the CTL events (Figs. 4, 7, and 12). In addition, comparisons of the MJO composites from the two simulations show that the CPL simulation has an increased amount of PBL specific humidity and PBL moisture convergence leading the development of deep convection and lagging the systematic development of warm SST produced from the coupled ocean mixed layer (Figs. 10, 12, and 13). This enhancement in PBL moisture provides an increase in the moist static energy available to the deep convective region. Determining the genesis for this increase in low-level moisture is important to understanding the underlying physics that is responsible for the increased MJO variability in the coupled simulation. A boundary

layer adjustment to the increase in SST ahead of the convection via latent heat flux does not seem to be at work given that the SST increases are too small to account for the size of the moisture increase observed (see section 3e) and because the moisture increase does not appear to coincide with an increase in latent heat flux. This leaves the possibility that the moisture enhancing mechanism may be dynamically induced.

Comparisons of the atmospheric dynamic and latent heating fields from both simulations indicate that there is an enhanced low-level convergence leading the convection (Figs. 14 and 15). The underlying cause of this enhanced convergence appears to be due to a strengthening of the meridional surface convergence. Figures 16 and 17 show the zonally lagged correlations between PBL moisture convergence and surface temperature, surface moist static energy, surface zonal wind convergence, and surface meridional wind convergence for the CTL and CPL simulations, respectively. The correlations were computed from composites whose selection longitude varied between 100° and 150°E (horizontal axis; see section 3b), and for lags between ± 12 model grid points. Comparison of the upper left panels of the two figures emphasizes the main distinguishing feature between these two simulations, namely, the interactive

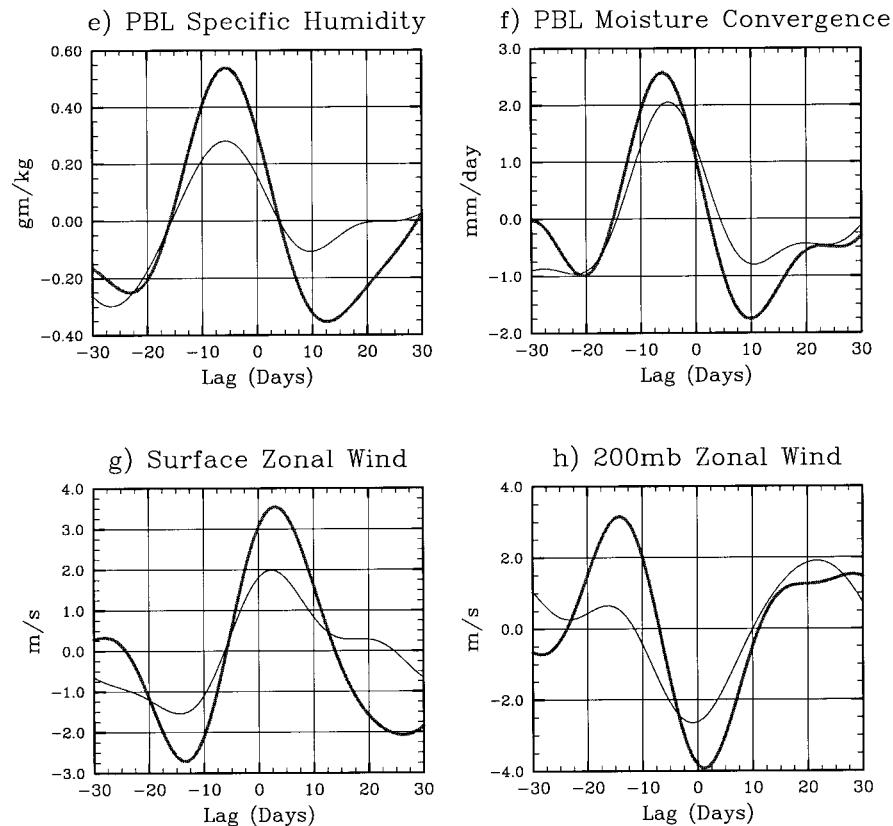


FIG. 13. (Continued) those diagrams, that is, an average of data between 145° and 155°E . (a) Surface latent heat flux, (b) net surface shortwave flux, (c) net surface flux, (d) surface temperature, (e) PBL specific humidity, (f) PBL moisture convergence, (g) surface zonal wind, and (h) 200-mb zonal wind.

SST introduced by the slab ocean mixed layer and the resulting SST warming (cooling) extending to the east (west) of the MJO rainfall anomaly. The relatively weaker and more unorganized relationship shown in the CTL correlations is based on land surface temperatures only, and in this case the model representations of equatorial Indonesia and New Guinea.

Comparison of the upper right panels of Figs. 16 and 17 emphasizes what has been demonstrated above (Figs. 12 and 13) regarding a more coherent relationship in the CPL simulation between the MJO convection anomaly and the PBL moisture (illustrated here in terms of PBL convergence and surface moist static energy). Interestingly, a comparison between the lower left panels of the two figures illustrates that very little change has occurred with regards to the strength or lead-lag relationship between zonal wind convergence and PBL moisture convergence. Both correlation plots show that PBL moisture convergence is closely associated with in situ zonal wind convergence (i.e., with little or no zonal lag). Comparison of the lower right panels shows a somewhat different relation between PBL moisture and meridional wind convergences in the CPL and CTL simulations. The correlation plot for the CTL simulation

shows that meridional wind convergence is also closely associated with PBL moisture convergence, with only a modest enhancement at most positive (i.e., eastward) zonal lags (i.e., dv/dy leads PBL moisture convergence). The correlation plot for the CPL simulation shows a more coherent relation between these two quantities and, contrary to the CTL plot, shows a correlation that generally maximizes when the meridional convergence leads the PBL moisture convergence. The difference in these two relationships suggests that the meridional wind convergence appears to be responsible for the increase in boundary layer moist energy leading the convection that is found in the CPL simulation (upper right panels).

Comparing the upper left and lower right panels shows that the SST signal leads or is in phase with the meridional convergence signal for the composites constructed at longitudes 100°E to about 130°E . In this region, it would appear that the meridional gradients in SST help to directly reinforce the meridional convergence east of the convection (i.e., Lindzen and Nigam 1987). However, east of about 140°E , the PBL moisture convergence tends to be more closely in phase with the SST anomaly, and the surface meridional convergence

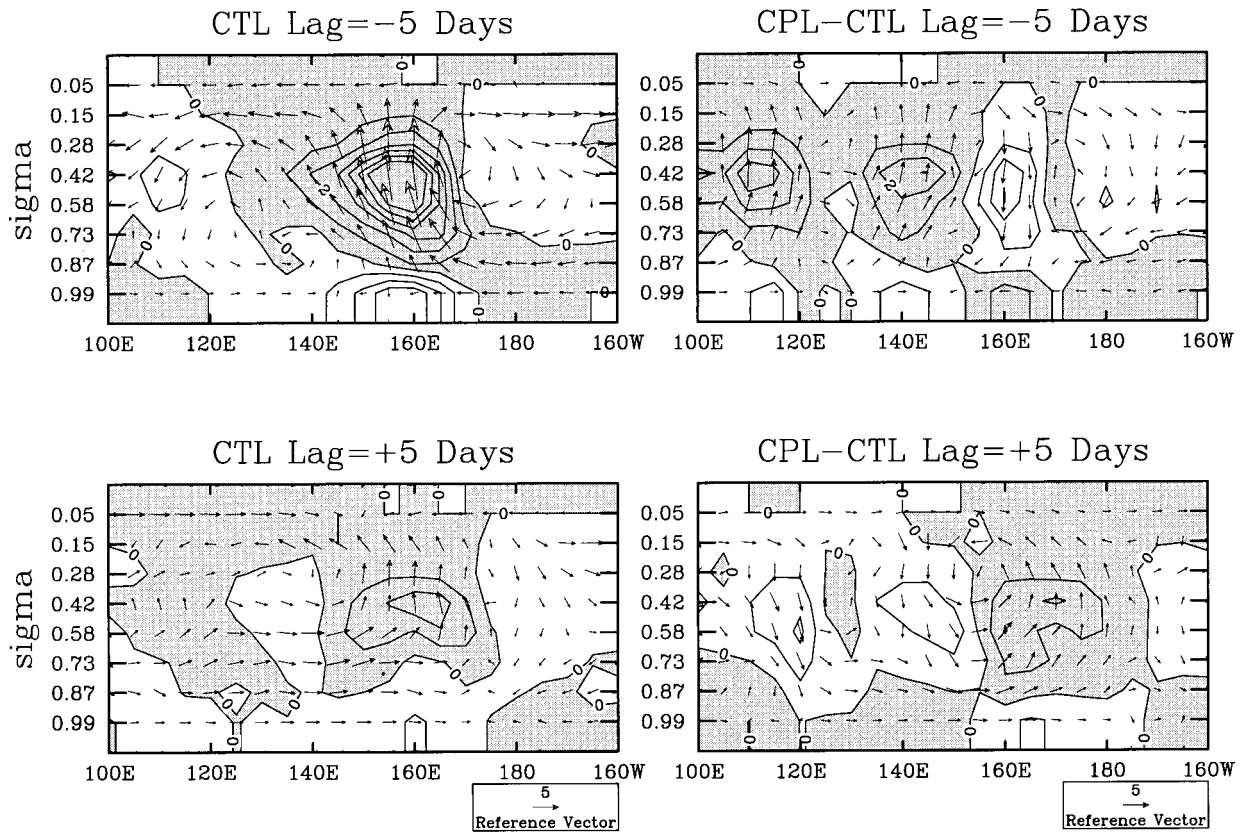


FIG. 14. Similar to Fig. 4, except for the composite values of equatorial vertical and horizontal velocity (vectors) and latent heating (contours) between 100°E and 160°W. The left panels show the equatorial values at lag -5 days (top) and +5 days (bottom), while the right panels show the difference between the CPL composites at these same time lags and the CTL composites. The reference vector indicates 5 m s⁻¹ horizontal velocity and 50 mb day⁻¹ vertical velocity. Contour interval for heating is 1° day⁻¹.

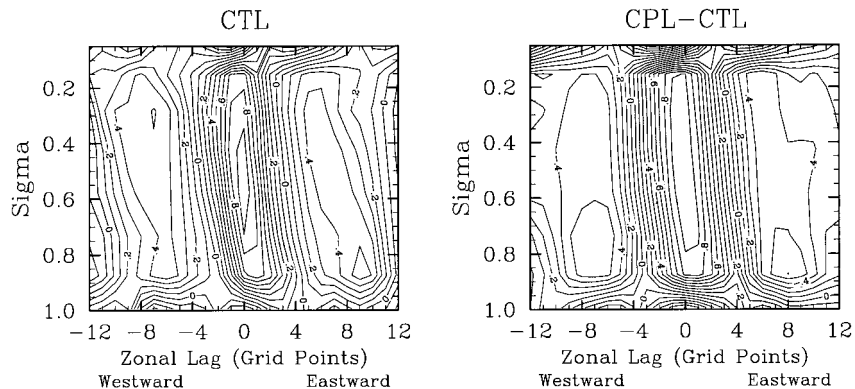


FIG. 15. Zonally lagged correlations between the midtropospheric vertical velocity and the vertical velocity at all levels for the CTL simulation (left), and the difference in this quantity between the CPL and CTL simulations (right). The computations are based on the same CTL and CPL composite data shown in Fig. 14, using the longitude range 100°E–160°W and time lags from -15 to +15 days. For each day (i.e., time lag), the vertical velocity at $\sigma = 0.58$ is correlated to the vertical velocity at all sigma levels, allowing the zonal lag to vary between ± 12 model grid points. Then each of these correlations maps (sigma vs zonal lag) are ensemble averaged together. Positive zonal lags indicate eastward, negative indicate westward. Contour interval is 0.1 and positive values are shaded.

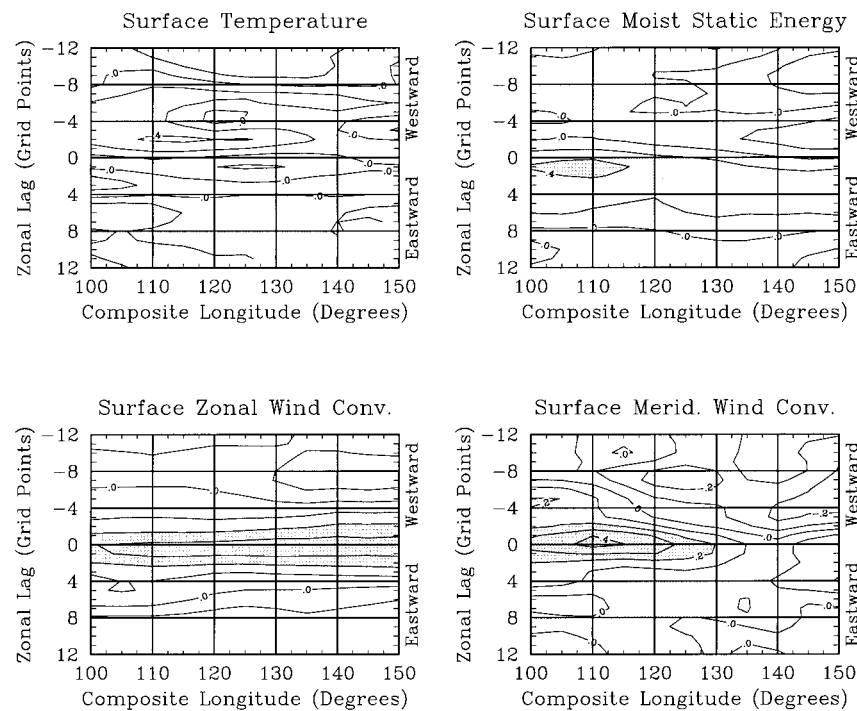


FIG. 16. Zonally lagged correlations between planetary boundary layer (PBL; $\sigma = 0.94\text{--}1.0$) moisture convergence and surface temperature (upper left), surface moist static energy (upper right), surface zonal wind convergence (lower left), and surface meridional wind convergence (lower right) for the CTL simulation. The correlations were computed from composites whose selection longitude varied between 100° and 150°E (horizontal axis; see section 3b), and for lags between ± 12 model grid points. Positive zonal lags indicate eastward, negative indicate westward. Contour interval is 0.2 (except for lower right, which is 0.1) and positive values are shaded.

leads both (meridional convergence is high to the east of the PBL moisture convergence). In this region, it is not obvious what is the cause of the enhanced meridional convergence. One hypothesis is that the earlier synchronization between the increased SST, meridional wind convergence, moist static energy, and convection has already enhanced the strength of the entire MJO complex, which in turn would force more (internal) latent heat-driven frictional convergence ahead of the convection. This would imply that over the course of the Eastern Hemisphere, the interaction between the SST and the atmospheric component of the MJO is not zonally uniform. This aspect is one of the directions we plan to pursue in future research. It is worth noting that the above interactions appear to be at work to the west of the convection center as well (i.e., at negative zonal lags). In regions behind the PBL moisture convergence maximum, there is a more robust relationship between negative SST anomalies, surface meridional divergence, and diminished moist static energy, with again little modification to the relationship with surface zonal wind convergence.

The analysis and discussion presented above provides some evidence for the positive impact an interactive SST has on a numerical simulation of the MJO and outlines

a plausible scenario for the manner coupled SSTs might be influencing the MJO in the observed system. It is noteworthy that the numerical study by Flatau et al. (1997) also found an increased strength and organization of the model's intraseasonal variability when coupling to SST was introduced. In their study, a simplified five-layer GCM (i.e., Lau et al. 1989) using the convection scheme of Emanuel (1991) showed intraseasonal variability that was too fast and dominated by wavenumbers one and two. Introduction of a slab ocean mixed layer and a highly idealized surface heat budget to the model promoted more realistic intraseasonal variability, namely, by slowing down the propagation speed and promoting a wavenumber-one selection. From these experiments, they hypothesized a new conceptual model referred to as "air-sea convective intraseasonal interaction" (ASCII), whereby the generated "zonal SST gradient causes zonal changes in surface moist static energy and provides surface forcing, promoting the development of convection in the convergent regions." While the basic premise of their results are the same as those presented here, Flatau et al. did not elaborate on the mechanism by which the moist static energy in their model is increased via the introduction of SSTs (e.g., surface heat fluxes, zonal/meridional moisture conver-

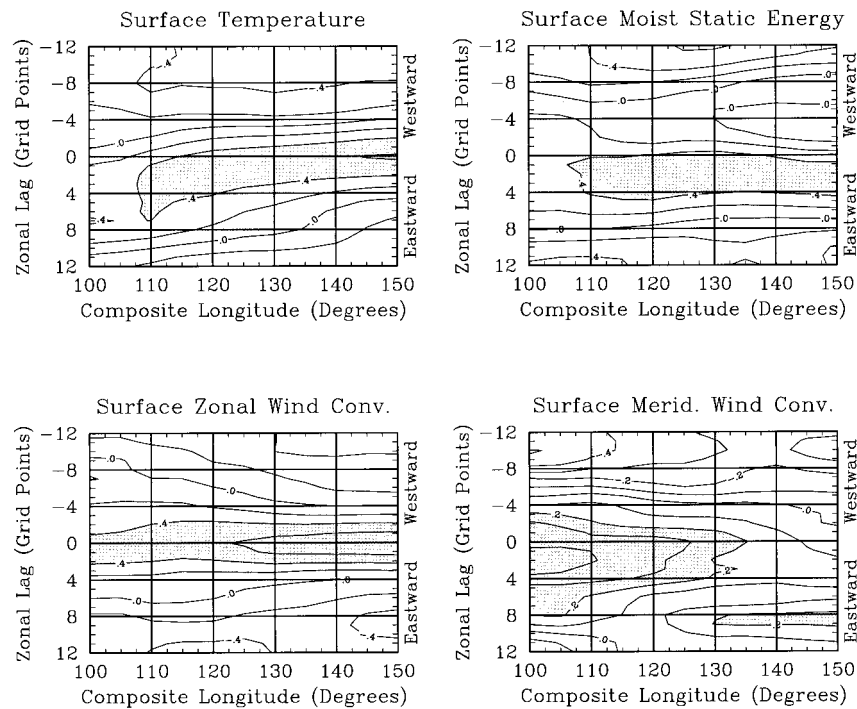


FIG. 17. Same as Fig. 16, except for CPL simulation.

gence). This question concerning the dominant mechanisms influencing the moisture supply east of the convection was raised by Sperber et al. (1997) as well in their comparison of fixed-SST model simulations to observations. The results of the present study suggest that meridional moisture convergence associated with frictional wave-CISK, acting in concert with the SST anomalies, is at least one of the key processes leading to the enhancement in moist static energy available for the eastward propagating convection. It is worth mentioning that in the case where an enhanced MJO circulation does develop (e.g., Fig. 14), the increased subsidence ahead of the wave may better inhibit small-scale convection, allowing the associated moisture to build up rather than be released prematurely. This might be a second-order process that helps enhance the moist static energy ahead of the convection. These questions deserve considerably more research before the answer can be demonstrated with significant certainty.

Given the improvements to the MJO in the simulation with coupled SSTs, the question arises whether the MJO should more accurately be considered an ocean-atmosphere coupled mode as suggested by Flatau et al. (1997) and Sperber et al. (1997). As mentioned in the introduction, a number of studies have hypothesized a feedback between SST and the MJO, but does such an interaction imply that the MJO is a true “coupled mode” of variability? The theoretical coupled ocean-atmosphere model developed by Wang and Xie (1998) exhibits high-frequency MJO-like unstable modes only when coupling to the ocean mixed layer is active. The

instability is induced primarily by the wind-entrainment–evaporation feedback and to a lesser extent by the cloud–radiation feedback, with little or no influence from ocean dynamics. The results of the Wang and Xie study would argue that the MJO is a coupled mode, in the strict sense that ENSO is a coupled ocean–atmosphere mode. If the MJO is a true coupled mode, then numerical and theoretical models that simulate disturbances similar to the MJO without an interactive SST (e.g., the CTL simulation) must be exaggerating or distorting marginally stable modes in the atmosphere that have a strong resemblance to the observed MJO. On the other hand, if the MJO inherently stems from an atmospheric instability that is enhanced through its interaction with a coupled SST, then the Wang and Xie theory could be marginalizing the atmospheric instability to the point where it is no longer unstable unless the ocean feedback is activated. At this point, the evidence more strongly supports the latter of these two scenarios (i.e., the MJO is an inherent instability of the atmospheric system, which is modified by its interaction with SST), given the vast number of different models, without coupling to SST, that contain an element of variability strongly resembling the MJO.

5. Summary

In this study, we document the changes in the MJO of two 10-yr GCM simulations using the GLA GCM. In the control (CTL) simulation, the SSTs are specified to be the annual cycle. The coupled (CPL) simulation

employs a 50-m slab ocean mixed layer equatorward of 24° latitude to compute SST anomalies that are added to the mean annual cycle of SSTs and thus coupled to the model atmosphere during the integration. The results show that while the two long-term model climatologies are very similar, the simulated MJO variability shows considerable differences. The principle difference is that the CPL simulation exhibits larger, and slightly more organized, MJO variability than the CTL simulation. This is evident in the overall increase in the number of events present (Figs. 5 and 6), the more robust and organized signal exhibited in the CPL composite event versus the CTL composite event (Figs. 4, 7, 12, 15), and the increased power ($\sim 40\%$) at 50–60 days in the wavenumber-one 200-mb velocity potential and surface zonal wind spectra (Fig. 7). In addition to this increased power, several variables (e.g., 200-mb VP and zonal wind, rain rate, and surface zonal wind) show a better consolidation of the wavenumber-one and/or -two variance around the two primary timescales evident in the observations (Fig. 7). Another interesting difference is that time–longitude MJO composite events from the western equatorial Pacific show that the slab mixed layer coupling slows the 200-mb velocity potential propagation in the Eastern Hemisphere from about 13 to 7 m s^{-1} (Fig. 4). Finally, the intraseasonal variability in the CPL simulation increased in a manner that enhanced its overall seasonality, with relatively more events occurring in the northern winter and spring seasons (Fig. 6).

Based on the recent AMIP comparison of the MJO variability in 15 GCMs performed by Slingo et al. (1996), all of the above differences suggest an improvement in the simulation relative to the observed MJO variability. Thus, to the extent that the CPL simulation does indeed represent an improvement in the model's representation of the MJO and its relationship to SST, it appears that feedback from an interactive SST may be one important factor in achieving better simulations of observed intraseasonal variability. Such a conclusion has important ramifications for the theoretical treatment of the MJO, as well as for medium-to-extended-range numerical weather prediction. Presently, there are few theoretical treatments of the MJO that incorporate even a simplified interactive SST (cf. Lau and Shen 1988; Hirst and Lau 1991), and only one (Wang and Xie 1998) that attempts to explicitly account for effects of both the surface latent heat flux and shortwave flux, as well as ocean mixing, on the evolution of the SST. From the model results presented here, the inclusion of an interactive SST (even a highly idealized one) results in a systematic increase (decrease) in SSTs to the east (west) of the convection. These changes in SST are primarily due to enhanced surface shortwave flux to the east of the convection, diminished shortwave flux coincident with the convection, and enhanced latent heat flux to the west of the convection. The enhanced SST to the east of the convection appears to reinforce the meridional convergence associated with the frictional wave–

CISK mechanism at work within the model. This in turn transports more PBL moisture into the region lying just east of the maximum PBL moisture convergence, which is dominated by zonal wind convergence. This increase in moist static energy helps destabilize the disturbance and/or maintain it against dissipation more effectively relative to a case without such SST coupling (see discussion in section 4). We would like to point out that several of the MJO modifications documented in this study are qualitatively similar to those found in the theoretical study of Wang and Xie (1998) (e.g., increased instability and slower propagation; see section 3b). However, their model does not explicitly treat moisture or account for the frictional part of wave–CISK, and thus it is not obvious as yet how analogous the similarities are between these results.

We would like to emphasize that taken in total, the differences between the two simulations were quite dramatic, and yet the systematic changes in SST tended to be very small, on the order of 0.10° – 0.15°C . It was by design that the SST perturbations were to be kept small. This helps ensure that the background climates of the two simulations remain the same and thus any resulting changes in the MJO characteristics between the two simulations could more readily be attributed to the MJO-organized SST fluctuations, rather than due to indirect changes from an altered climatological state. Comparisons of the climatologies from the two simulations, both the long-term means (Figs. 1 and 2) and the seasonal means (not shown) indicate that the changes were in generally less than 10% of the means, with the exception of a spatial reorganization of rainfall in the equatorial Indian and western Pacific Oceans (about 10%–20% of the means), which was largely induced by the changes in the intraseasonal variability itself (Figs. 8 and 9). Thus to the extent that we were successful in performing the perturbation experiment we intended, the results indicate a significant sensitivity of the model's MJO to coupled SST variability. With this in mind, it is worth mentioning again that of the models that tended to perform the best in the MJO comparison study by Slingo et al. (1996) all exhibited a positive relationship between increasing rainfall and increasing SST that was at least as strong as that exhibited by observed data. In this regard, the GLA model may have been a particularly good candidate model for the experiment described here.

The simplified model framework and perturbation type experiment employed in this study also circumvent the problem alluded to above as it would apply to comparing extant simulations from fully coupled ocean–atmosphere models to their fixed-SST counterparts. In short, the authors know of no coupled models that have a coupled climatology sufficiently close to their forced climatology to offer results that could be used to discriminate the interactive-SST effects alone on the MJO. As discussed in section 2, the differences in the MJO between a fixed and fully coupled simulation will likely be overwhelmed by the differences in the climatology

of which the MJO is highly sensitive to (e.g., Salby and Hendon 1994; Wang and Rui 1990b; also Fig. 5). One avenue around this problem might be to perform a coupled simulation first, and then use the prognostic SST, or its climatology, from this simulation as a specified boundary condition in a fixed-SST simulation. In this way, both simulations would have the same climatological state and the effects from the coupled SST could be better determined.

With respect to the possible impact the above results have on medium- to extended-range midlatitude weather forecasts, Chen and Alpert (1990) showed that when the MJO amplitude is large, model forecast skill of MJO propagation and amplitude were quite good out to 10 days. However, when the MJO amplitude was small, the forecast skill was poor. Similarly, Ferranti et al. (1990) demonstrated that the skills of medium- to extended-range forecasts in the extratropics are significantly improved when the errors associated with the representation of the tropical intraseasonal oscillation are minimized. More recently, Lau and Chang (1992) analyzed one season (14 December 1986–31 March 1987) of 30-day global forecasts derived from the NCEP Dynamical Extended Range Forecasts. Their results showed that the NCEP forecast model has significant skill in predicting the global pattern of intraseasonal variability up to 10 days, with the error growth of tropical and extratropical low-frequency modes less (greater) than persistence when the amplitude of the MJO is large (small). Based on the results of these forecast and predictability studies and the suggestion in this study that an interactive SST may improve the simulation quality, including increasing its magnitude and altering its phase speed in the Eastern Hemisphere, it is possible that the incorporation of a simplified, interactive SST in NWP models may improve extended-range weather forecasts. We are presently collaborating with NCEP personnel to examine this hypothesis.

Acknowledgments. Support for this study was provided by the Climate Dynamics Program in the Atmospheric Sciences Division of the National Science Foundation under Grants ATM-9420833 and ATM-9712483 (DW), the National Oceanic and Atmospheric Administration's Pan American Climate Study Program Grant NA56GP0236 (DW), and Dr. K. Bergman of the NASA Mission to Planet Earth Office (WL and JK). The authors would like to thank Charles Jones (UCSB) for providing the observed pentad values of OLR and SST, Wesley Berg (CDC/NOAA) for providing the mean GPCP rainfall data, and Greg Walker (Goddard/NASA) for help with the GLA model and providing the model output from the control run. We would further like to thank three anonymous reviewers for their comments, which helped to improve the overall presentation of the paper. This study's analysis greatly benefited from the use of the TeraScan software analysis system, a product of SeaSpace Corporation, San Diego, California.

REFERENCES

- Arakawa, A., and W. H. Schubert, 1974: Interaction of a cumulus cloud ensemble with the large scale environment, Part I. *J. Atmos. Sci.*, **31**, 674–701.
- , and V. R. Lamb, 1977: Computational design of the basic dynamical processes of the UCLA general circulation model. *Methods in Computational Physics*, J. Chang, Ed., Vol. 17. Academic Press, 173–265.
- Chang, C. P., 1977: Viscous internal gravity waves and low-frequency oscillations in the Tropics. *J. Atmos. Sci.*, **34**, 901–910.
- , and H. Lim, 1988: Kelvin wave–CISK: A possible mechanism for the 30–50 day oscillation. *J. Atmos. Sci.*, **45**, 1709–1720.
- Chao, W. C., 1995: A critique of wave–CISK as an explanation for the 40–50 day tropical intraseasonal oscillation. *J. Meteor. Soc. Japan*, **73**, 677–684.
- Chen, T.-C., and M. Murakami, 1988: The 30–40 day variation of convective activity over the western Pacific Ocean with emphasis on the northwestern region. *Mon. Wea. Rev.*, **116**, 892–906.
- , and J. C. Alpert, 1990: Systematic errors in the annual and intraseasonal variations of the planetary-scale divergent circulation in NMC medium-range forecasts. *Mon. Wea. Rev.*, **118**, 2607–2623.
- , R. Y. Tzeng, and M. C. Yen, 1988: Development and life cycle of the Indian monsoon: Effect of the 30–50 day oscillation. *Mon. Wea. Rev.*, **116**, 2183–2199.
- Crum, F. X., and T. J. Dunkerton, 1994: CISK and evaporation–wind feedback with conditional heating on an equatorial beta-plane. *J. Meteor. Soc. Japan*, **72**, 11–18.
- Emanuel, K. A., 1987: An air–sea interaction model of intraseasonal oscillations in the Tropics. *J. Atmos. Sci.*, **44**, 2324–2340.
- , 1988: Reply. *J. Atmos. Sci.*, **45**, 3528–3530.
- , 1991: A scheme for representing cumulus convection in large-scale models. *J. Atmos. Sci.*, **48**, 2313–2335.
- Ferranti, L., T. N. Palmer, F. Molteni, and K. Klinker, 1990: Tropical–extratropical interaction associated with the 30–60-day oscillation and its impact on medium and extended range prediction. *J. Atmos. Sci.*, **47**, 2177–2199.
- Flatau, M., P. J. Flatau, P. Phoebus, and P. P. Niiler, 1997: The feedback between equatorial convection and local radiative and evaporative processes: The implications for intraseasonal oscillations. *J. Atmos. Sci.*, **54**, 2373–2386.
- Gates, W. L., 1992: AMIP: The Atmospheric Model Intercomparison Project. *Bull. Amer. Meteor. Soc.*, **73**, 1962–1970.
- , and A. B. Nelson, 1975: A new (revised) tabulation of the Scripps topography on a one-degree global grid. Part 1: Terrain heights. Rand Tech. Rep. R-1276-1-ARPA, The Rand Corporation, Santa Monica, CA, 132 pp.
- Gray, W., 1988: Seasonal frequency variations in the 40–50 day oscillation. *Int. J. Climatol.*, **8**, 511–519.
- Harshvardhan, R. Davies, D. A. Randall, and T. G. Corsetti, 1987: A fast radiation parameterization for general circulation models. *J. Geophys. Res.*, **92**, 1009–1016.
- Hayashi, Y., and D. G. Golder, 1993: Tropical 40–50 and 25–30-day oscillations appearing in realistic and idealized GFDL climate models and ECMWF dataset. *J. Atmos. Sci.*, **50**, 464–494.
- Helfand, H. M., and J. C. Labraga, 1988: Design of a non-singular level 2.5 second order closure model for prediction of atmospheric turbulence. *J. Atmos. Sci.*, **45**, 113–132.
- Hendon, H. H., 1988: A simple model of the 40–50 day oscillation. *J. Atmos. Sci.*, **45**, 569–584.
- , and B. Liebmann, 1990a: A composite study of onset of the Australian summer monsoon. *J. Atmos. Sci.*, **47**, 2227–2240.
- , and —, 1990b: The intraseasonal (30–50-day) oscillation of the Australian summer monsoon. *J. Atmos. Sci.*, **47**, 2909–2923.
- , and M. L. Salby, 1994: The life cycle of the Madden and Julian oscillation. *J. Atmos. Sci.*, **51**, 2225–2237.
- , and —, 1996: Planetary-scale circulations forced by intraseasonal variations of observed convection. *J. Atmos. Sci.*, **53**, 1751–1758.

- , and J. Glick, 1997: Intraseasonal air–sea interaction in the tropical Indian and Pacific Oceans. *J. Climate*, **10**, 647–661.
- Hirst, A., and K.-M. Lau, 1990: Intraseasonal and interannual oscillations in coupled ocean–atmosphere models. *J. Climate*, **3**, 713–725.
- Hu, Q., and D. A. Randall, 1994: Low-frequency oscillations in radiative-convective systems. *J. Atmos. Sci.*, **51**, 1089–1099.
- , and —, 1995: Low-frequency oscillations in radiative-convective systems. Part II: An idealized model. *J. Atmos. Sci.*, **52**, 478–490.
- Huffman, G. J., and Coauthors, 1997: The Global Precipitation Climatology Project (GPCP) Combined Precipitation Dataset. *Bull. Amer. Meteor. Soc.*, **78**, 5–20.
- Jones, C., and B. C. Weare, 1996: The role of low-level moisture convergence and ocean latent heat fluxes in the Madden–Julian oscillation: An observational analysis using ISCCP data and ECMWF analyses. *J. Climate*, **9**, 3086–3104.
- , D. E. Waliser, and C. Gautier, 1998: The influence of the Madden–Julian oscillation on ocean surface heat fluxes and sea surface temperatures. *J. Climate*, **11**, 1057–1072.
- Kalnay, E., R. Balgovind, W. Chao, D. Edelman, J. Pfendner, L. Takacs, and K. Takano, 1983: Documentation of the GLAS fourth order general circulation model, Volume I. NASA Tech. Memo. 86064, NASA/Goddard Space Flight Center, Greenbelt, MD, 436 pp. [Available from NASA/Goddard Space Flight Center, Greenbelt, MD 20771.]
- , and Coauthors, 1996: The NCEP/NCAR 40-year Reanalysis Project. *Bull. Amer. Meteor. Soc.*, **77**, 437–471.
- Kawamura, R., 1988: Intraseasonal variability of sea surface temperatures over the tropical western Pacific. *J. Meteor. Soc. Japan*, **66**, 1007–1012.
- , 1991: Air–sea coupled modes on intraseasonal and interannual time scales over the tropical western Pacific. *J. Geophys. Res.*, **96**, 3165–3172.
- Kessler, W. S., M. J. McPhaden, and K. M. Weickmann, 1996: Forcing of intraseasonal Kelvin waves in the equatorial Pacific. *J. Geophys. Res.*, **100**, 10 613–10 631.
- Kirtman, B., and A. Vernekar, 1993: On wave–CISK and the evaporation–wind feedback for the Madden–Julian Oscillation. *J. Atmos. Sci.*, **50**, 2811–2814.
- Knutson, T. R., and K. M. Weickmann, 1987: The 30–60 day atmospheric oscillation: Composite life cycles of convection and circulation anomalies. *Mon. Wea. Rev.*, **115**, 1407–1436.
- Krishnamurti, T. N., D. K. Oosterhof, and A. V. Metha, 1988: Air–sea interaction on the timescale of 30 to 50 days. *J. Atmos. Sci.*, **45**, 1304–1322.
- Lau, K.-M., and P. H. Chan, 1983: Short-term climate variability and atmospheric teleconnections from satellite-observed outgoing longwave radiation. Part I: Simultaneous relationships. *J. Atmos. Sci.*, **40**, 2735–2750.
- , and —, 1985: Aspects of the 40–50 day oscillation during the northern winter as inferred from outgoing longwave radiation. *Mon. Wea. Rev.*, **113**, 1889–1909.
- , and —, 1986: Aspects of the 40–50 day oscillation during the northern summer as inferred from outgoing longwave radiation. *Mon. Wea. Rev.*, **114**, 1354–1367.
- , and T. J. Phillips, 1986: Coherent fluctuations of extratropical geopotential height and tropical convection in intraseasonal timescales. *J. Atmos. Sci.*, **43**, 1164–1181.
- , and L. Peng, 1987: Origin of low-frequency (intraseasonal) oscillations in the tropical atmosphere. Part I: Basic theory. *J. Atmos. Sci.*, **44**, 950–972.
- , and P. H. Chan, 1988: Intraseasonal and interannual variations of tropical convection: A possible link between the 40–50 day oscillation and ENSO? *J. Atmos. Sci.*, **45**, 506–521.
- , and S. Shen, 1988: On the dynamics of intraseasonal oscillations and ENSO. *J. Atmos. Sci.*, **45**, 1781–1797.
- , and F. C. Chang, 1992: Tropical intraseasonal oscillation and its prediction by the NMC operational model. *J. Climate*, **5**, 1365–1378.
- , and C. H. Sui, 1997: Mechanisms of short-term sea surface temperature regulation: Observations during TOGA COARE. *J. Climate*, **9**, 465–472.
- , L. Peng, C. H. Sui, and T. Nakazawa, 1989: Dynamics of super cloud clusters, westerly wind bursts, 30–60 day oscillations and ENSO: A unified view. *J. Meteor. Soc. Japan*, **67**, 205–219.
- , T. Nakazawa, and C. H. Sui, 1991: Observations of cloud cluster hierarchies over the tropical western Pacific. *J. Geophys. Res.*, **96**, 3197–3208.
- Lau, N. C., I. M. Held, and J. D. Neelin, 1988: The Madden–Julian oscillation in an idealized general circulation model. *J. Atmos. Sci.*, **45**, 3810–3832.
- Legeckis, R., 1977: Long waves of the eastern equatorial Pacific Ocean: A view from a geostationary satellite. *Science*, **197**, 1179–1181.
- Li, T. M., and B. Wang, 1994: The influence of sea surface temperature on the tropical intraseasonal oscillation: A numerical study. *Mon. Wea. Rev.*, **122**, 2349–2362.
- Liebmann, B., and D. L. Hartmann, 1984: An observational study of tropical–midlatitude interaction on intraseasonal timescales during winter. *J. Atmos. Sci.*, **41**, 3333–3350.
- , H. H. Hendon, J. D. Glick, and J.-K. E. Schemm, 1997: An assessment of the skill of forecasts made using the NCEP reanalysis model, including those initialized during active and inactive periods of the Madden–Julian Oscillation. *Proc. 22d Annual Climate Diagnostics and Prediction Workshop*, Berkeley, CA, National Oceanic and Atmospheric Administration, 345–346.
- Lin, X., and R. H. Johnson, 1996: Kinematic and thermodynamic characteristics of the flow over the western Pacific warm pool during TOGA COARE. *J. Atmos. Sci.*, **53**, 695–715.
- Lindzen, R. S., and S. Nigam, 1987: On the role of sea surface temperature gradients in forcing low-level winds and convergence in the Tropics. *J. Atmos. Sci.*, **44**, 2418–2436.
- Lord, S. J., and A. Arakawa, 1980: Interaction of a cumulus cloud ensemble with the large-scale environment. Part II. *J. Atmos. Sci.*, **37**, 2677–2692.
- Madden, R. A., and P. R. Julian, 1971: Detection of a 40–50 day oscillation in the zonal wind in the tropical Pacific. *J. Atmos. Sci.*, **28**, 702–708.
- , and —, 1994: Observations of the 40–50-day tropical oscillation: A review. *Mon. Wea. Rev.*, **122**, 814–837.
- McPhaden, M. J., 1996: Monthly period oscillations in the Pacific North Equatorial Countercurrent. *J. Geophys. Res.*, **101**, 6337–6359.
- , and B. A. Taft, 1988: Dynamics of seasonal and intraseasonal variability in the eastern equatorial Pacific. *J. Phys. Oceanogr.*, **18**, 1713–1732.
- Murakami, T., 1976: Cloudiness fluctuations during the summer monsoon. *J. Meteor. Soc. Japan*, **54**, 175–181.
- Nakazawa, T., 1986: Intraseasonal variations in the OLR in the Tropics during the FGGE year. *J. Meteor. Soc. Japan*, **64**, 17–34.
- , 1995: Intraseasonal oscillations during the TOGA-COARE IOP. *J. Meteor. Soc. Japan*, **73**, 305–319.
- Neelin, J. D., 1988: Reply. *J. Atmos. Sci.*, **45**, 3526–3527.
- , I. M. Held, and K. H. Cook, 1987: Evaporation–wind feedback and low-frequency variability in the tropical atmosphere. *J. Atmos. Sci.*, **44**, 2341–2348.
- Phillips, T. J., 1996: Documentation of the AMIP models on the World Wide Web. *Bull. Amer. Meteor. Soc.*, **77**, 1191–1196.
- Salby, M. L., and H. H. Hendon, 1994: Intraseasonal behavior of clouds, temperature and motion in the tropics. *J. Atmos. Sci.*, **51**, 2207–2224.
- , R. Garcia, and H. H. Hendon, 1994: Planetary circulations in the presence of climatological and wave-induced heating. *J. Atmos. Sci.*, **51**, 2344–2367.
- Sellers, P. J., Y. Mintz, Y. C. Sud, and A. Dalcher, 1986: A simple biosphere model (SiB) for use within general circulation models. *J. Atmos. Sci.*, **43**, 505–531.

- Shapiro, R., 1970: Smoothing, filtering and boundary effects. *Rev. Geophys. Space Phys.*, **8**, 359–387.
- Slingo, J. M., and Coauthors, 1996: Intraseasonal oscillations in 15 atmospheric general circulation models: Results from an AMIP diagnostic subproject. *Climate Dyn.*, **12**, 325–357.
- Spencer, R. W., 1993: Global oceanic precipitation from the MSU during 1979–91 and comparisons to other climatologies. *J. Climate*, **6**, 1301–1326.
- Sperber, K. R., J. M. Slingo, P. M. Inness, and K. M. Lau, 1997: On the maintenance and initiation of the intraseasonal oscillation in the NCEP/NCAR Reanalysis and the GLA and UKMO AMIP simulations. *Climate Dyn.*, **13**, 769–795.
- Sud, Y. C., and G. K. Walker, 1992: A review of recent research on improvement of physical parameterizations in the GLA GCM. *Physical Processes in Atmospheric Models*, D. R. Sikka and S. S. Singh, Eds., Wiley Eastern Ltd., 422–479.
- , W. C. Chao, and G. K. Walker, 1991: Contributions to the implementation of Arakawa-Schubert cumulus parameterizations in the GLA GCM. *J. Atmos. Sci.*, **48**, 1573–1586.
- , —, and —, 1992: Role of a cumulus parameterization scheme in maintaining atmospheric circulation and rainfall in the nine-layer Goddard Laboratory for Atmospheres General Circulation Model. *Mon. Wea. Rev.*, **120**, 594–611.
- Van den Dool, H. M., 1994: Long-range weather forecasts through numerical and empirical methods. *Dyn. Atmos. Oceans*, **20**, 247–270.
- Waliser, D. E., 1996: Formation and limiting mechanism for very high SST: Linking the dynamics and thermodynamics. *J. Climate*, **9**, 161–188.
- , N. E. Graham, and C. Gautier, 1993: Comparison of the highly reflective cloud and outgoing longwave data sets for use in estimating tropical deep convection. *J. Climate*, **6**, 331–353.
- , W. D. Collins, and S. P. Anderson, 1996: An estimate of the surface shortwave cloud forcing over the western Pacific during TOGA COARE. *Geophys. Res. Lett.*, **23**, 519–522.
- Wang, B., 1988a: Dynamics of the tropical low-frequency waves: An analysis of the moist Kelvin wave. *J. Atmos. Sci.*, **45**, 2051–2065.
- , 1988b: Comments on “An air–sea interaction model of intraseasonal oscillation in the Tropics.” *J. Atmos. Sci.*, **45**, 3521–3525.
- , and H. Rui, 1990a: Dynamics of the coupled moist Kelvin–Rossby wave on an equatorial beta plane. *J. Atmos. Sci.*, **47**, 397–413.
- , and —, 1990b: Synoptic climatology of transient tropical intraseasonal convection anomalies. *Meteor. Atmos. Phys.*, **44**, 43–61.
- , and X. Xie, 1998: Coupled modes of the warm pool climate system. Part I: The role of air–sea interaction in maintaining Madden–Julian Oscillation. *J. Climate*, **11**, 2116–2135.
- Weickmann, K., M., 1983: Intraseasonal circulation and outgoing longwave radiation modes during Northern Hemisphere winter. *Mon. Wea. Rev.*, **111**, 1838–1858.
- , 1991: El Niño/Southern Oscillation and Madden–Julian (30–60 day) oscillations during 1981–1982. *J. Geophys. Res.*, **96**, 3187–3195.
- , G. R. Lussky, and J. E. Kutzbach, 1985: Intraseasonal (30–60 day) fluctuations of outgoing longwave radiation and 250 mb stream function during northern winter. *Mon. Wea. Rev.*, **113**, 941–961.
- Weller, R. A., and S. A. Anderson, 1996: Temporal variability and mean values of the surface meteorology and air–sea fluxes in the western equatorial Pacific warm pool during TOGA COARE. *J. Climate*, **9**, 1959–1990.
- Xue, Y.-K., P. J. Sellers, J. L. Kinter II, and J. Shukla, 1991: A simplified biosphere model for global climate studies. *J. Climate*, **4**, 345–364.
- Yasunari, T., 1979: Cloudiness fluctuations associated with the Northern Hemisphere monsoon. *J. Meteor. Soc. Japan.*, **58**, 225–229.
- , 1980: A quasi-stationary appearance of the 30–40 day period in the cloudiness fluctuations during the summer monsoon over India. *J. Meteor. Soc. Japan.*, **59**, 336–354.
- Zhang, C., 1996: Atmospheric intraseasonal variability at the surface in the tropical western Pacific Ocean. *J. Atmos. Sci.*, **53**, 739–758.
- , and H. H. Hendon, 1997: On propagating and standing components of the intraseasonal oscillation in tropical convection. *J. Atmos. Sci.*, **54**, 741–752.
- Zhang, G. J., and M. J. McPhaden, 1995: On the relationship between sea surface temperature and latent heat flux in the equatorial Pacific. *J. Climate*, **8**, 589–605.